Journal of Environmental Chemical Engineering 13 (2025) 114996

Contents lists available at ScienceDirect

Journal of Environmental Chemical Engineering

journal homepage: www.elsevier.com/locate/jece

Magnetic biochar generated from oil-mill wastewater by microwave-assisted hydrothermal treatment for sonocatalytic antibiotic degradation

Pengyun Liu [a,1], Zhilin Wu [b,1,*], Maela Manzoli [a], Giancarlo Cravotto [a,*]

[a] Department of Drug Science and Technology, University of Turin, via P. Giuria 9, Turin 10125, Italy
[b] College of Chemistry and Chemical Engineering of Shantou University, and Chemistry and Chemical Engineering Guangdong Laboratory, Shantou 515063, PR China

ARTICLE INFO

Keywords:
Magnetic biochar
Oil-mill wastewater treatment
Microwave-assisted hydrothermal process
Sonocatalytic degradation
Antibiotics

ABSTRACT

The pollution risks of biomass-containing and antibiotics-containing wastewater mean that it must be treated before discharge into the environment. In a process following circular economy principles, oil-mill wastewater (OMWW) was treated in a microwave-assisted hydrothermal process and with simultaneously fabricated magnetic biochar (MBC), which was used as a catalyst for the sonocatalytic degradation of antibiotics metronidazole (MET) and ciprofloxacin (CIP) in aqueous solutions. $FeCl_3{\cdot}6H_2O$, $FeCl_2{\cdot}4H_2O$, and KOH were added to the OMWW, which was then treated in a SynthWave microwave reactor under either a nitrogen or air atmosphere. The UV_{254} and COD removal efficiencies of the OMWW reached 42.3% and 60.6%, respectively, after treatment at 250 °C for 3 h. The MBC obtained from the OMWW treatment with air exhibited the highest adsorption and catalytic activity for antibiotics degradation. The synergistic effects of combining adsorption and sonolytic removal were in the ranges of 0.76–3.07 (MET) and 0.75–3.17 (CIP), resulting in significant degradation rate constants of pseudo-first-order kinetics (k_1) that ranged from 0.010 to 0.086 min^{-1} (MET) and from 0.018 to 0.050 min^{-1} (CIP). Hydrophobic MET underwent faster degradation than hydrophilic CIP. The $^{\bullet}OH$ is crucial for removing the model antibiotics. Initial antibiotics concentration, reaction volume, ultrasonic frequency, and power had clearer impacts on antibiotics degradation than bulk temperature. Furthermore, the possible sonocatalytic degradation pathways have also been proposed herein. The absorbents and catalysts were derived during the purification of OMWW and subsequently used for antibiotics removal from water, becoming an innovative case of circular economy and sustainable waste treatment.

1. Introduction

Antibiotics (ABX) are known to prevent the spread and growth of microorganisms (*e.g.* bacteria, protozoans, microalgae, viruses, and fungi), and have thus been consumed in their tons, and observed in a range of water environments in various concentrations in recent decades [1–3]. The presence of ABX in water may lead to the formation of resistance genes in bacteria, weak crop development, poor organism metabolism, and pose severe health risks to human beings, *e.g.* serious allergic reactions, toxic effects (nephrotoxicity, hematological toxicity, *etc.*), imbalance in the intestinal flora and damage to the immune system [4,5]. The common ABX metronidazole (MET, a nitroimidazole ABX) and ciprofloxacin (CIP, a fluoroquinolone ABX) have been widely used to cure anaerobic infections and microbial diseases in humans and animals [6–8]. MET and CIP have recently been used to prevent and treat COVID-19 infections [9,10]. Both MET and CIP enter water environments via the discharge involved in their production as well as via human and animal excrement and can be persistent in water matrices. The residual concentrations of MET and CIP in water environments have been reported to range from ng L^{-1} to μg L^{-1} [11–13]. It is therefore

Abbreviations: ABX, antibiotics; BC, biochar; BET, Brunauer-Emmett-Teller; CIP, ciprofloxacin; COD, chemical oxygen demand; *DEs*, degradation efficiencies; EDS, energy dispersive X-ray spectroscopy; FESEM, field emission scanning electron microscopy; FT-IR, Fourier-transform infrared spectroscopy; MBCs, magnetic BC-based materials; MET, metronidazole; OMWW, oil mill wastewater; MW, microwave; PXRD, powder X-ray diffraction; ROS, reactive oxygen species; SE, synergistic effects; TDS, total dissolved solids; TGA, thermogravimetric analysis; TS, total solids; TSS, total suspended solids; US, ultrasound; *RT*, retention time.

* Corresponding authors.
E-mail addresses: zhlwu@stu.edu.cn (Z. Wu), giancarlo.cravotto@unito.it (G. Cravotto).

[1] These authors shared co-first authorship.

https://doi.org/10.1016/j.jece.2024.114996
Received 6 October 2024; Received in revised form 24 November 2024; Accepted 29 November 2024
Available online 30 November 2024

necessary to develop appropriate ways to remove ABX from water environments.

Advanced oxidation processes, which involve the strongly oxidative hydroxyl radical ($^{\bullet}$OH), have been popular in the field of wastewater purification in recent decades [14]. These processes, including ozonation, Fenton, photochemical, sonochemical, electrochemical, *etc.*, have been widely used for degrading ABX in water [8,13,15–17]. However, several drawbacks are restricting their application. For instance, ozonation is generally energy-consuming and ozone reacts with unsaturated substrates selectively. The Fenton process is relatively expensive due to the requirements of large chemical doses, while the recovery of Fenton reagents is difficult. Although photochemical processes are convenient in their operation, the relevant degradation efficiencies (*DEs*) of contaminants strongly depend on light-source configuration, limitations in mass transfer, and a narrow operation range of pH, *etc*. Sonication alone is generally a low-efficiency approach with poor ABX mineralization. Similarly, electrochemical processes are usually energy-consuming and high-cost [16]. By contrast, sonolytic processes that are enhanced by various catalysts have attracted a great deal of attention due to their excellent performance in degrading ABX in water [18–20]. Generally, the synergistic effect (*SE*) of adsorption over catalysts and ultrasonication (US) plays a decisive role in heterogeneous sonocatalytic systems. On the one hand, sonication triggers both physical and chemical effects, in which numerous cavitational bubbles are generated, expanded, imploded, and are accompanied by high temperatures (approx. 5000 K), high pressures (approx. 500 atm), cumulative micro-jets (approx. 10 m s^{-1}), and sonoluminescence, *etc.* [21], while $^{\bullet}$OH are generated during the collapse of cavities, inducing a series of radical-based oxidative reactions [14,22]. On the other hand, adding catalysts to sonolytic systems can enhance the degradation of ABX by intensifying the cavitational effects, forming more reactive oxygen species (ROS), as well as by providing more active sites on the catalysts. Additionally, catalysts can maintain stable effectiveness as sonication continuously refreshes their surfaces [19,21,23].

Materials, including carbon-rich materials, metal oxides, and the relevant composites, *etc.*, have been synthesized and used as sonocatalysts for ABX removal from water [23–25]. Compared to single carbon-rich materials or metal oxides, the composites provide better sonocatalytic performance [25–31]. Carbon-rich materials generally possess high specific surface areas and pore volume, rich-pore textures, and good adsorption capacity, providing abundant reaction sites for the adsorption and *in-situ* oxidative degradation of ABX, while metal oxides can also create micro-battery effects and generate free radicals by homogeneous cleavage of peroxide bonds via the single electron transfer pathway [23,26]. Biochars (BCs) are carbon-rich materials, possessing a wide source of precursors and high mechanical strength, *etc.* [16,32]. BCs could be produced via biomass pyrolysis under limited oxygen conditions regarding the properties essentially associated with the pyrolysis temperature, the components of precursors, reaction environments, *etc.* [33]. However, BCs often have poor separation from liquid matrices and low recycling efficiency followed by limited applications [24,32]. Magnetic BC-based materials (MBCs) can not only improve the separation of BCs but also intensify their sonocatalytic efficiency and reduce the degradation costs by reusing the consumed MBCs [18–20, 25–29,31]. MBCs can be fabricated by either loading metal or their oxide, nanoparticles (*e.g.* iron, Fe_2O_3, Fe_3O_4, α-Fe_2O_3, Fe_2NO_3, $Fe_2(SO_4)_3$, *etc.*) onto BCs [11,15,30,32,34–36].

Conventional approaches such as pyrolysis, gasification, torrefaction, and flash carbonization have been used for biochar production with limitations of high energy-intensive (up to 900 °C) and low economy [37]. In contrast, hydrothermal synthesis can produce biochar by directly conversing high humidity biomass or dry precursors with water under relevant mild subcritical conditions (generally 180–250 °C and 20–60 bar) through a series of reactions including hydrolysis, pyrolysis, dehydration, decarboxylation, decarbonylation, re-condensation, polymerization, *etc.* [38,39]. Compared with conventional pyrolysis, hydrothermal synthesis is convenient for treating biomass precursors in a larger range with higher biochar yield and smaller waste gas production [40]. Compared with the conventionally synthesized biochar, the hydrothermally synthesized biochar (or hydrochar) possesses higher labile carbons, lower aromaticity structure, and lower ash content, while the main components are both cellulose, hemicellulose, and lignin. Moreover, the hydrothermally synthesized biochar has an equivalence ratio of H: C and O: C as compared with natural coal, while higher than the conventionally synthesized biochar [41–43]. It has been reported that more O-containing functional groups, *e.g.* phenolic, carboxylic, hydroxyl, and carbonyl existed in the outer surface of hydrothermally synthesized biochar, which exhibited highly dispersed in aqueous solutions favoring acting as sonocatalysts [44–46]. On the other hand, both microwave (MW) and conventional heating have been used to prepare BCs and their composites [25–31,47,48]. MW irradiation can more rapidly and selectively heat the carbon-containing polar particles by dipole rotation and ionic conduction, and creates numerous 'hot spots', increasing the disruption of biomass materials [49,50]. Compared with the traditional approach, MW exhibits distinctive benefits such as high efficiency, low energy consumption, and loss, uniform heat transfer, high yields, low risk of pore blockage, *etc.* [51]. The electromagnetic component of MW were reported to be able to directly interact with biomass, which is beneficial in producing uniform particle size owing to the rapid synthesizing of small crystals followed by a compacting particle size distribution [50,52–54]. Moreover, MW heating can also improve the C/O ratio of materials by changing the proportion of O-containing functional groups [47]. MW-assisted hydrothermal synthesis thus shares the benefits of both MW heating and hydrothermal treatment with the decomposition rate of biomass 10 times faster than conventional heating [55]. Although several biochars or MBCs have been fabricated via similar MW-assisted hydrothermal synthesis, the current work shows novelty in the constant reaction pressure, changeable gas filling, stable magnetic stirring, much smaller additional precursors (only 0.03 g) and solvents, as well as the free of further activation. Moreover, the prepared MBCs act as both adsorbents and catalysts [56–59].

Against this backdrop, MBCs have been innovatively synthesized herein via the MW-assisted hydrothermal treatment of oil-mill wastewater (OMWW) with $FeCl_2{\cdot}4H_2O$ and $FeCl_3{\cdot}6H_2O$ under either nitrogen or air atmosphere. To implement the circular economy approach, the purification of OMWW, to a certain degree, and MBC preparation were simultaneously achieved. Meanwhile, the prepared MBCs can be used as a catalyst to perform the sonocatalytic degradation of MET and CIP in water. A range of catalysts has been characterized using field emission scanning electron microscopy (FESEM) combined with energy dispersive X-ray spectroscopy (EDS), powder X-ray diffraction (PXRD), N_2 physisorption at lid nitrogen temperature, Brunauer-Emmett-Teller (BET) analysis, thermogravimetric analysis (TGA), and Fourier-transform infrared spectroscopy (FT-IR). After MW-assisted hydrothermal treatment, the quality of OMWW was also evaluated. The sonocatalytic degradation of MET and CIP in aqueous solutions, via various processes, was optimized in terms of catalyst dose, additives, initial ABX concentration, reaction volume, ultrasonic power and frequency, and bulk temperature. Finally, possible pathways for the sonocatalytic degradation of MET and CIP have also been proposed.

2. Materials and methods

2.1. Materials, chemicals and apparatus

Detailed information on the chemicals used in this study is shown in Section S1. The chemical structure and physicochemical properties of MET and CIP are shown in Table S1. An ultrasonic cleaner (35 kHz, Fisherbrand, Singen/Htw., Germany) was used to homogenize the matrix. A pH microprocessor (Hanna instruments, pH 211) was used to measure the pH of matrices. The high-frequency (500 kHz) device

consists of an ultrasonic generator (UMC-Premium, Weber Ultrasonics, Germany). At the maximum electrical output power of 318 W, the corresponding ultrasonic power was detected, by calorimetry, to be 259 W. In addition, a multi-frequency device (MG 200, Weber Ultrasonics, Germany), consisting of a sonic digital generator (operating at variable frequencies of 40, 80, and 120 kHz), was used in this study, and the ultrasonic power, corresponding to the maximum electrical output power of 150 W, was detected to be 87 W by calorimetry. Detailed information on these ultrasonic devices has been shown in our previous studies [23,60]. A digital thermometer with a pointed probe (Hanna instruments, HI 98501) was used to monitor bulk temperature. A SynthWave MW reactor (Milestone Srl, Italy) was used for MW-assisted hydrothermal synthesis. A freeze-drier (LyoQuest-85 lyophilizer, Azbil Telstar Technologies, Spain) was used for the analysis of total solids (TS) and total dissolved solids (TDS) in OMWW. A liquid phase parallel synthesizer (Heidolph Synthesis 1, Germany) was used to perform the adsorption of ABX onto the prepared materials in aqueous solutions. The TGA and FT-IR of the prepared samples were performed using a Thermogravimetric Analyser (TGA 4000, PerkinElmer) and an FT-IR Spectrometer (Spectrum Two, PerkinElmer), respectively. Other methods for the characterization of OMWW and of the prepared materials have been described in detail in Section S2.

2.2. Treatment of OMWW and biochar preparation

OMWW was treated using various methods (a-d), and a range of different materials were simultaneously fabricated under optimal conditions:

a) Centrifugation: 100 mL of OMWW was centrifuged at 4200 rpm for 30 min to obtain the total suspended solids (*TSS*), which are labeled as TSS_0;

b) US/MW treatment: 80 mL of OMWW was previously sonicated in a cleaner bath at 35 kHz for 30 min and divided equally into 8 portions without pH adjustment. Aliquots (10 mL) of the processed OMWW were added into eight 20 mL test tubes and reacted in an MW-assisted hydrothermal process under either nitrogen (labeled as BC-N_2) or air (labeled as BC-Air) atmosphere at 250 °C and 80 bar for 3 h;

c) US/MW treatment under basic conditions: the pH value of 30 mL of OMWW was previously adjusted to 10 using KOH solutions. Afterward, the mixture was sonicated at 35 kHz for 30 min and divided equally into 3 portions. Aliquots (10 mL) of the processed OMWW were respectively added to three 20 mL test tubes and reacted in an MW-assisted hydrothermal process under either nitrogen (labeled as BC-N_2-pH 10) or air (labeled as BC-Air-pH 10) atmosphere at 250 °C and 80 bar for 3 h;

d) US/MW treatment with Fe(II)/Fe(III) compounds under basic conditions: a 0.03 g mixture of $FeCl_3{\cdot}6H_2O$ and $FeCl_2{\cdot}4H_2O$ (mol/mol, 2:1) was previously added to 80 mL of OMWW and sonicated at 35 kHz for 10 min. The pH value of the mixture was adjusted to 10 using KOH solutions and sonicated at 35 kHz for 30 min. Afterward, the mixture was divided equally into 8 portions, and aliquots (10 mL) of the processed OMWW were added into eight 20 mL test tubes, which were reacted in an MW-assisted hydrothermal process under either nitrogen atmosphere (labeled as MBC-N_2) for 3 h or an air atmosphere (labeled as MBC-Air) for 3 h at 250 °C and 80 bar. Details of the procedure for treating OMWW and preparing MBCs are shown in Fig. 1.

Upon processes b, c, and d, the pH values of the mixture were adjusted to neutral using H_2SO_4 solution. The obtained biochars were washed several times using distilled water to remove any possible water-soluble impurities and were dried in an oven at 100 °C overnight. The final products were collected for the subsequent experiments.

2.3. Sonocatalytic degradation of MET and CIP in aqueous solution

In a typical run, adsorption was previously performed by mixing 50 mL of either 30.2 μM MET or CIP aqueous solutions with a 5 mg catalyst, the mixture was shaken at 500 rpm for 30 min at room temperature to reach adsorption-desorption equilibrium (Table S2). To carry out sonocatalytic degradation, the above mixture, after adsorption, was transferred to a 1-L Erlenmeyer flask, which was set over the serpentine condenser (at approx. 1 cm from the bottom) in the sonication reactor and sonicated at 500 kHz and 259 W ultrasonic power in an ambient atmosphere at pH 7 and room temperature. The bulk temperature was continuously monitored and controlled by cooling water during sonication. Water samples were withdrawn periodically and then centrifuged to obtain the supernatants, which were analyzed using an HPLC system. The used catalyst can be separated from the reaction systems via both centrifugation and magnetic separation and regeneration under MW irradiation.

2.4. Determination of model ABX and intermediates

MET and CIP were analyzed using a UPLC-MS/MS system (Acquity TQD LC/MS/MS System, Waters Corporation, Milford, MA, USA) equipped with Gemini C-18 column (5 μm, 4.6 ×100 mm) via isocratic elution using 0.1% TFA in H_2O (Phase A) and 0.1% TFA in MeCN (Phase

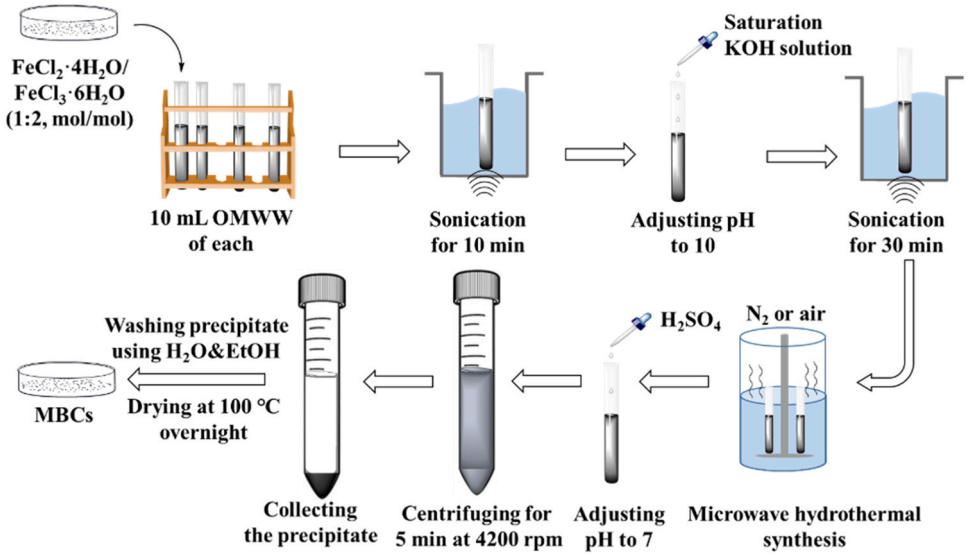

Fig. 1. The procedure of OMWW treatment and MBC preparation in a MW-assisted hydrothermal process.

B) at room temperature. The flow rate and injection volumes were 1 mL min^{-1} and 40 μL, respectively. The isocratic elution for MET (or CIP) was carried out using 70% (or 80%) Phase A and 30% (or 20%) Phase B for 15 min (or 10 min). Intermediates from MET and CIP were identified using a UPLC-MS/MS system equipped with a Kinetex C18 column (5 μm, 150 × 4.6 mm) and an electrospray ion source operated in positive ionization mode. Isocratic elution was performed with 80% Phase A and 20% Phase B at a flow rate of 1 mL min^{-1} for 28 min with an injection volume of 20 μL.

2.5. Evaluation of ABX removal

In order to evaluate removal kinetics and efficiency, the pseudo-first-order (PFO) model constant (k_1, min^{-1}), pseudo-second-order model constant (k_2, L mg^{-1} min^{-1}), and the *DE* (%) of ABX were calculated, according to Eqs. (1)-(3) [61,62]:

$$\frac{C_t}{C_0} = e^{-k_1 t} \quad (1)$$

$$\frac{1}{C_t} - \frac{1}{C_0} = k_2 t \quad (2)$$

$$DE\ (\%) = \frac{C_0 - C_t}{C_0} \times 100 \quad (3)$$

where C_0 (mg L^{-1} or μM) is the initial ABX concentration and C_t (mg L^{-1} or μM) is the ABX concentration at a given time t (min). All experiments were performed in duplicate and errors are given by the difference between the highest measured value and the average value of the paired treatments. Where errors are not visible in the figures, they are smaller than the symbols representing the average values.

2.6. Analysis of OMWW and characterization of prepared biochars

The methods for the analysis of OMWW and the characterization of the prepared biochars are described in Section S2.

3. Results and discussion

3.1. MW-assisted hydrothermal treatment of OMWW

The indicators of wastewater quality, *e.g.* the pH, the absorbance of light at a wavelength of 254 nm (UV_{254}, cm^{-1}), the chemical oxygen demand (COD, g L^{-1}), and the oil content (g L^{-1}), for the OMWWs before and after treatment are summarized in Table 1.

In addition, the analyzed oil contents, TS, TSS, and TDS in the original OMWW were 0.06%, 4.75%, 0.73%, and 3.96%, respectively. The obvious sediment was observed in the original OMWW, and the color of the surfactant suggests that some solutes were included in the supernatant (Fig. 2a).

Table 1
Quality indicators of OMWWs before and after treatment.

Samples	*Indicators*				
	pH	*UV_{254} (cm^{-1})*	*COD (g L^{-1})*	*TSS (g L^{-1})*	*BC yield (g L^{-1})*
Original OMWW	5.48	[a]164.5	[b]136	7.28	0
OMWW(BC-N_2)	5.62	117.8	-	0	13.6
OMWW(BC-Air)	5.55	154.2	-	0	14.0
OMWW(BC-N_2-pH 10)	10	109.7	-	0	14.2
OMWW(BC-Air-pH 10)	10	143.9	-	0	16.5
OMWW(MBC-N_2)	10	94.9	53.6	0	14.5
OMWW(MBC-Air)	10	134.9	70.4	0	12.0

Note: OMWW(BC-N_2), OMWW(BC-Air), OMWW(BC-N_2-pH 10), OMWW(BC-Air-pH 10), OMWW(MBC-N_2) and OMWW(MBC-Air) stand for the supernatants obtained during the preparation of BC-N_2, BC-Air, BC-N_2-pH 10, BC-Air-pH 10, MBC-N_2 and MBC-Air, respectively.

[a] *UV_{254}* value was calculated in terms of the detection of the 2500-fold-diluted OMWW.

[b] *COD* value was calculated in terms of the detection of the 500-fold-diluted OMWW.

10 mL of the original OMWW were centrifuged to obtain the supernatant and sediment (*i.e.* TSS_0), where the quality indicators in the obtained supernatant are the same as those in the original OMWW, apart from the TSS value. TSS_0 was used as the blank catalyst of the various BCs for the sonocatalytic degradation of MET and CIP. A 30 mg mixture of $FeCl_3{\cdot}6H_2O$ and $FeCl_2{\cdot}4H_2O$ (mol/mol, 2:1), under basic conditions, was previously added to 10 mL of OMWW, which was then sonicated (Fig. 2b). The sonicated mixture was treated in the MW-assisted hydrothermal process, (d) in Section 2.2, and the appearance of the collected supernatant is shown in Fig. 2c. The color of the sample in Fig. 2b likely results from the formation of Fe(II)/Fe(III) compounds. Nevertheless, the color of the sample in Fig. 2c is much lighter than the previous two samples, demonstrating that OMWW had undergone significant purification. Based on Table 1, UV_{254} values after the MW-assisted hydrothermal treatment are ordered as OMWW(BC-Air) > OMWW(BC-Air-pH 10) > OMWW(MBC-Air) > OMWW(BC-N_2) > OMWW(BC-N_2-pH 10) > OMWW(MBC-N_2). Good linear correlations between UV_{254} and COD in organic wastewater have been reported in one of our previous works, indicating that the UV_{254} value of the various samples in Table 1 can be used as references for the corresponding COD values [63].

The *DEs* of UV_{254} reached 42.3% and 18.0% under N_2 and air atmospheres, respectively, while the relevant *DEs* of COD were 60.6% and 48.2%. The fact that the *DEs* of UV_{254} and COD under an air atmosphere are lower than those achieved under the N_2 atmosphere is probably a result of the produced soluble organics (such as organic acids, *etc.*) via oxidation in the presence of oxygen and derived reactive oxygen species contributed to higher COD and UV_{254} values. The lower yields of the magnetic BCs compared to the other BCs may be due to the generated BCs reacting with Fe(II)/Fe(III) compounds under the high temperature (250 °C) and pressure (80 bar). Moreover, the better OMWW purification results achieved under basic conditions may be caused by the improved carbonization of the biomass [47,51,64].

3.2. Characterization of the prepared BCs

3.2.1. FESEM analysis

The morphological features of TSS_0, BC-N_2, BC-Air, BC-N_2-pH 10, BC-Air-pH 10, MBC-N_2, and MBC-Air are shown in Fig. S1. Globular particle agglomerates are observed on all samples, according to the FESEM images in Fig. S1a-g. These morphologies are typical of non-saccharide constituents (*e.g.* lignins, and their decomposition products) and amorphous carbons formed during the MW-assisted

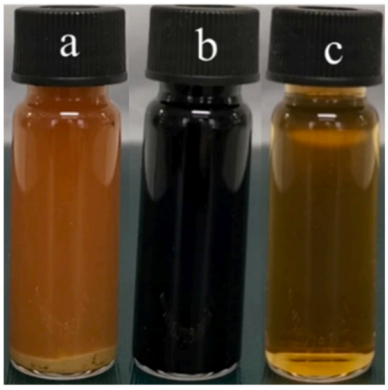

Fig. 2. The appearance of the original OMWW (a), 10 mL of OMWW with 0.03 g $FeCl_3{\cdot}6H_2O$ and $FeCl_2{\cdot}4H_2O$ (2:1, mol/mol) at pH 10 (b) and the supernatant collected after the MW-assisted hydrothermal treatment (c).

hydrothermal treatment. In particular, MBC-N_2 (Fig. S1f) and MBC-Air (Fig. S1g) possess smaller and less agglomerated particles homogeneous in size than the other materials, and this may be due to alternations to the synthesis and the growth patterns of the amorphous carbon when $FeCl_2{\cdot}4H_2O$ and $FeCl_3{\cdot}6H_2O$ are added [19,65]. In addition, C and O were identified using the EDS probe, in Fig. S2, and were found in all samples as the main elements.

3.2.2. EDS analysis

The large relative amount of C (54.4 wt%) in Fig. S2a indicates that OMWW is a suitable precursor for preparing BCs and MBCs. Based on the EDS analyses reported in Fig. S2b-g, the catalyst C relative contents are ordered as MBC-N_2 (69.0 wt%) > MBC-Air (66.0 wt%) > BC-Air-pH 10 (63.9 wt%) > MBC-N_2-pH10 (59.8 wt%) > BC-N_2 (32.0 wt%) > BC-Air (30.0 wt%), whereas the O relative amounts are ordered as BC-N_2 (39.1 wt%) > BC-Air (37.8 wt%) > BC-Air-pH 10 (24.6 wt%) > MBC-Air (24.3 wt%) > BC-N_2-pH 10 (21.6%) > MBC-N_2 (18.4%). These results indicate that an alkaline pH affects positively the carbonization of biomass, and it can be hypothesized that $FeCl_2{\cdot}4H_2O$ and $FeCl_3{\cdot}6H_2O$ may act as catalysts in the process. This is further confirmed by EDS analysis that put in evidence the presence of Fe only on the MBC-N_2 and MBC-Air materials (Fig. S2f and g), which supports the successful preparation of BC/Fe_3O_4 composites. These results are consistent with those related to the OMWW treatment in Section 3.1.

3.2.3. PXRD analysis and magnetism demonstration

The PXRD patterns of TSS_0, MBC-N_2, and MBC-Air are presented in Fig. 3a.

As shown in Fig. 3a, the broad diffraction peak at $2\theta = 20.55°$ in the PXRD pattern of TSS0, MBC-N_2, and MBC-Air, is related to the presence of amorphous carbon [66]. Moreover, weak diffraction peaks likely related to aluminum calcium magnesium silicate (JCPDS Card no. 00–004–0682) already present in the original matrix are observed in all PXRD patterns. Other peaks observed in the case of MBC-N_2 and MBC-Air (with higher intensity in the latter sample) at $2\theta = 30.1°$, 35.7° and 57.2°, are ascribed to the (220), (311) and (511) planes of magnetite in the cubic phase (JCPDS Card no. 00–001–1111), suggesting that the Fe_3O_4 spinel was formed and conserved during MW-assisted hydrothermal treatment [18,19]. The demonstration of the magnetic separation of MBC-Air from a MET solution is presented in Fig. 3b. As shown, the magnetism of MBC-Air facilitates its separation from reaction systems with the assistance of external magnetic action.

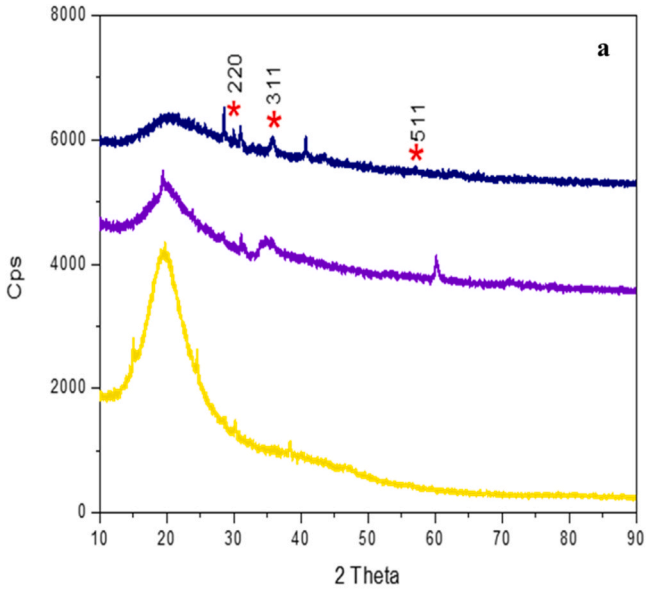

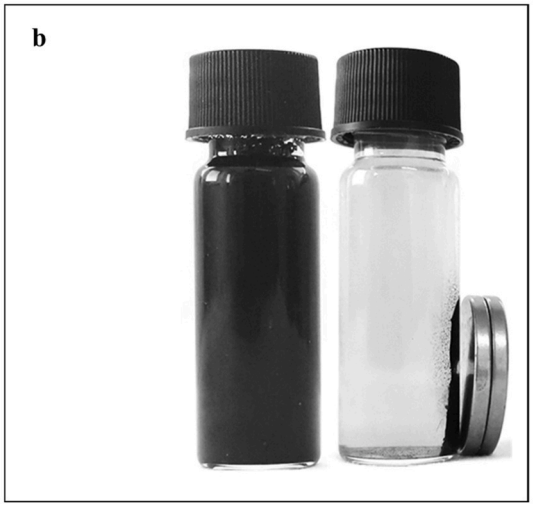

Fig. 3. PXRD patterns of TSS_0, MBC-N_2, and MBC-Air (a), appearance of dispersing 20 mg MBC-Air in MET aqueous solution (b, left) and separation of MBC-Air from MET aqueous solution using an external magnet (b, right).

3.2.4. TGA analysis

The TGA and derivative thermogravimetric curves of TSS_0, BC-N_2, BC-Air, BC-N_2-pH 10, BC-Air-pH 10, MBC-N_2, and MBC-Air are presented in Fig. 4a and b, respectively.

As shown in Fig. 4a, the weight losses of TSS_0, BC-N_2, BC-Air, BC-N_2-pH 10, BC-Air-pH 10, MBC-N_2, and MBC-Air range from 0.1 wt% to 2.0 wt% as the temperature rose from 35 to 120 °C, with this weight change being a result of the loss of moisture from the catalysts [24]. Accelerated weight losses in various samples were observed at 200–400 °C, where peak values reached at 320 (and 392), 330, 258, 258 (and 370), 232 (and 370), 224 and 219 °C for TSS_0, BC-N_2, BC-Air, BC-N_2-pH 10, BC-Air-pH 10, MBC-N_2, and MBC-Air, respectively (Fig. 4b). At 200–400 °C, the weight losses are ordered as follows: TSS_0 (61.9%) > BC-Air (46.2%) > BC-N_2-pH 10 (43.7%) > BC-N_2 (40.8%) > BC-Air-pH 10 (31.1%) > MBC-N_2 (24.2%) > MBC-Air (21.3%). When the temperature was further increased from 400 to 1000 °C, catalyst weight loss was ordered as follows: MBC-Air (42.2%) > BC-Air-pH 10 (32.5%) > MBC-N_2 (31.2%) > BC-N_2-pH 10 (24.8%) > BC-N_2 (21.6%) > TSS_0 (21.1%) > BC-Air (21.0%). These results put in evidence that most of the MBC weight loss occurred at 400–1000 °C, whereas in non-magnetic catalysts occurred between 200 and 400 °C. It has been reported that natural fibers decomposed first to hemicellulose, with then cellulose, lignin, and ash then being produced in sequence with increasing temperature [67]. The weight loss in the 200–400 °C range can thus be attributed to the decomposition of hemicellulose, cellulose, and other organics, *e.g.* fatty acids, glycosidic methylcellulose, *etc.* [36,68]. At 400–1000 °C, lignin was mainly decomposed to ash [69].

3.2.5. FT-IR spectroscopy analysis

FT-IR analysis favors the identification of the chemical bonds and surface groups of materials. The FT-IR spectra of the prepared TSS_0, BCs, and MBCs are shown in Fig. 4c. The proposed chemical bonds and functional groups are marked in the prepared spectra in Fig. 4c and summarized in Table S4. Peaks at 2924 and 2850 cm^{-1} provide evidence of the presence of -CH_2- groups, along with peaks at 721 and 1380 cm^{-1}, which reveal that there are long-chain saturated alkanes on the surface of all the prepared samples. Peaks at 1744 and 1715 cm^{-1} suggest that the surfaces include several C═O bond-containing groups. Peaks at 3010 cm^{-1} as well as at 1600, 1500, and 1450 cm^{-1} (and 700 cm^{-1}) correspond to the vibrations of the C-H and C═C bonds on the aromatic rings (or Ar-R on aromatic compounds). Peaks at 1000–1010 cm^{-1} and 1250–1275 cm^{-1} correspond to the stretching vibrations of -O- and Ar-O bonds, respectively. In addition, the peak at 570 cm^{-1} may be ascribed to the stretching vibration of Fe-O bonds in MBC-Air [18]. The proposed

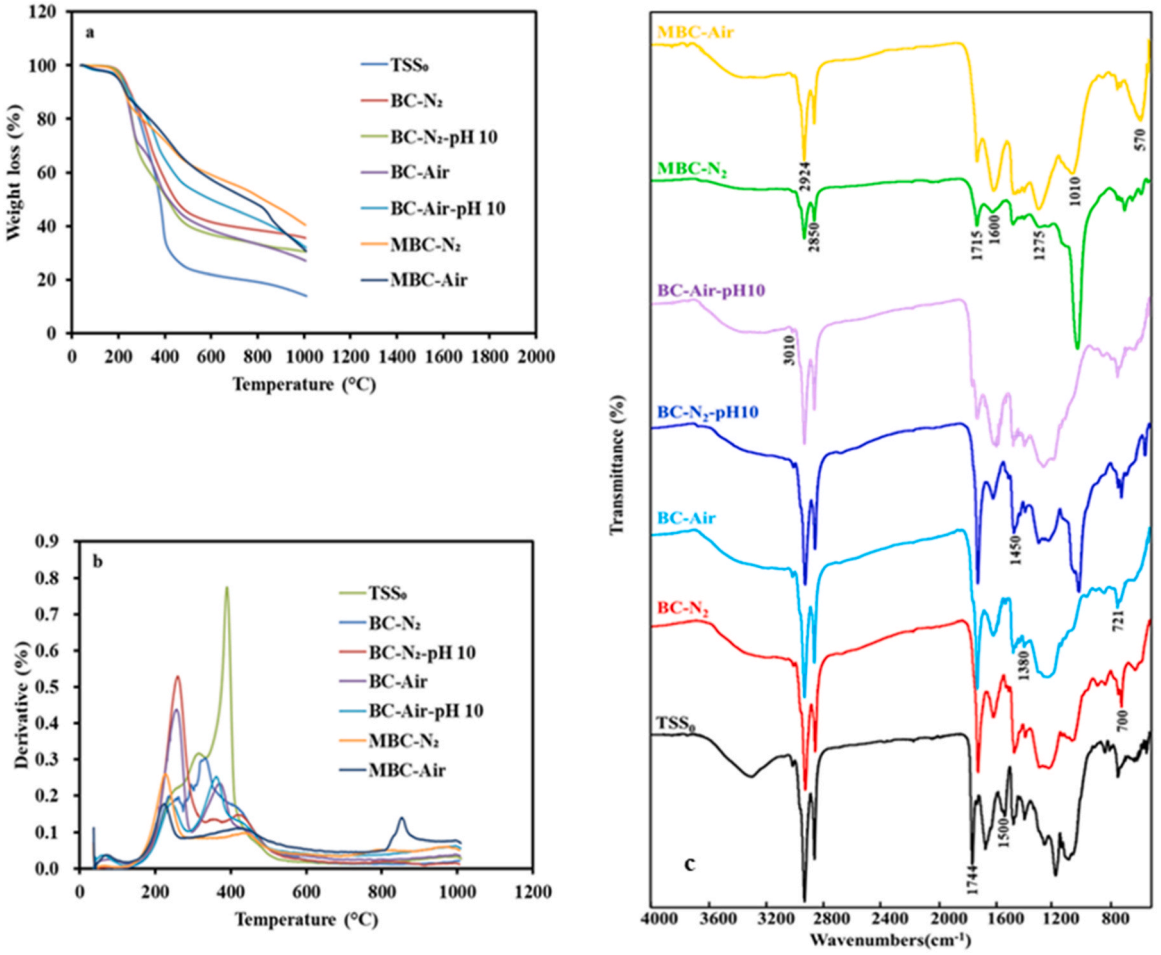

Fig. 4. The thermogravimetric (a) and derivative thermogravimetric (b) curves, and the FT-IR spectra (c) of the prepared materials.

assignment is in agreement with the fact that MBC-Air possesses better magnetic properties than MBC-N_2 and by XRD results, revealing that the peaks related to the magnetite crystalline phase are more evident on MBC-Air than on MBC-N_2.

3.2.6. *BET analysis*

The N_2 adsorption-desorption isotherms of MBC-N_2 and MBC-Air are shown in Fig. S3. As shown, these isotherms can be categorized as type IV with a type-H_4 hysteresis loop, referring to the IUPAC classification, and the differences in the isotherms suggest that MBC-Air possesses better porosity than MBC-N_2. The BET surface areas, mesopore volumes, and average pore diameters of MBC-N_2 and MBC-Air were measured to be 10.42 $m^2\ g^{-1}$, 0.029 $cm^3\ g^{-1}$, 11.14 nm and 13.89 $m^2\ g^{-1}$, 0.027 $cm^3\ g^{-1}$, 7.67 nm, respectively. These results prove that the prepared MBC-N_2 and MBC-Air are mesoporous (2–50 nm) materials, referring to the IUPAC classification. The low surface areas of MBC-N_2 and MBC-Air suggest low adsorption capacities towards the model ABX [47,51,70].

3.3. *Comparison of various processes in MET degradation*

To evaluate the contribution of various processes to removing MET, its degradation using adsorption, sonolysis, and sonocatalysis was investigated under the same operational conditions. 50 mL of a 30.2 μM (5.17 mg L^{-1}) MET solution was sonicated at 500 kHz and 259 W with or without 5 mg MBC-Air at pH 7. The results are shown in Fig. 5.

As shown in Fig. 5, the adsorption-desorption equilibrium was achieved in 30 min. The adsorption data in Table S2, acquired with the use of MBC-Air, were fitted using Freundlich and Langmuir adsorption

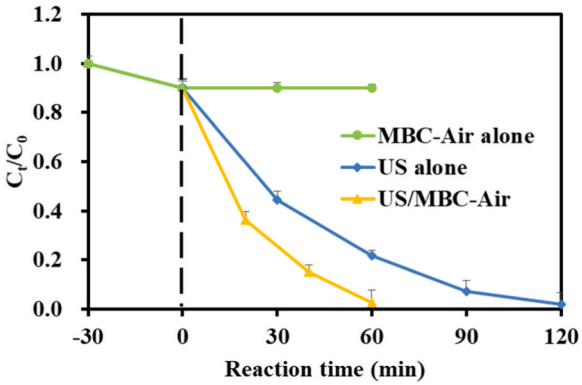

Fig. 5. Comparison of adsorption, sonication, and sonocatalysis with MBC-Air on the removal of MET (conditions: initial MET concentration before processing, 30.2 μM; reaction volume, 50 mL; dosage of MBC-Air, 0.1 g L^{-1}; US frequency, 500 kHz; US power, 259 W; pH 7, room temperature).

isotherm models, and the values of q_m, K_L, K_F, and $1/n$ are presented in Table S3. As shown, the adsorption of MET and CIP onto MBC-Air in aqueous solutions fits the Freundlich isotherm model well (R^2: 0.9706–0.9834). The high $1/n$ values (2.3862–2.5013) suggest that small amounts of MET and CIP are adsorbed onto MBC-Air [47].

Adding MBC-Air to the sonolytic system raised the *DE* of MET under the given conditions. The removal of MET from aqueous solutions using sonolysis and sonocatalysis follows pseudo-first-order kinetics well,

which is verified by high correlation coefficients (R^2: 0.9665–0.9936). 9.8%, 75.9%, and 96.9% MET was degraded by adsorption, sonication (k_1: 0.029 min^{-1}), and sonocatalysis (k_1: 0.053 min^{-1}), respectively, in 60 min. As a comparison, the relevant k_2 values of the model ABX degradation in Sections 3.3–3.6 are listed in Table S5 in detail. After sonocatalytic degradation, 143.9 $\mu g\ L^{-1}$ MET remained. The higher *DE* of MET achieved by sonocatalysis over sonolysis may be due to the generation of conduction band electron/valence band hole pairs, namely, e^-/h^+ pairs over the surface of MBC-Air, which can further induce the generation of ROS (*e.g.* $^{\bullet}OH$, $O_2^{\bullet-}$, $HO_2^{\bullet}$, *etc.*) and oxidative chemicals (*e.g.* H_2O_2, *etc.*) thanks to intrinsic charge separation via the pyrolysis of H_2O, radical reactions, as well as Fenton-like processes in sonocatalytic systems (Reactions S1–22) [20,36,71,72].

Moreover, the values of *SE* can be calculated from Eq. 4 [23]:

$$SE = \frac{k_{Sonocatalysis}}{k_{Adsorption} + k_{Sonication}} \quad (4)$$

where $k_{sonocatalysis}$, $k_{Adsorption,}$ and $k_{Sonication}$ are the degradation rates of ABX in sonocatalysis, adsorption, and sonication under the given conditions, respectively. Theoretically, synergism occurs between adsorption and sonolysis in sonocatalytic systems when the *SE* value is over 1.0.

Based on Eq. 1, the *SE* value between adsorption and sonication alone in MBC-Air-involved sonocatalysis is calculated to be 1.83, demonstrating that high synergism existed during the sonocatalytic degradation of MET.

3.4. Effects of catalyst type and dosage

To investigate the effect of catalyst type, 50 mL of 30.2 μM MET or CIP (*i.e.* 5.17 mg L^{-1} MET or 10.00 mg L^{-1} CIP) solutions were sonicated at 500 kHz and 259 W with 5 mg TSS_0, BC-N_2, BC-Air, BC-N_2-pH 10, BC-Air-pH 10, MBC-N_2 and MBC-Air at room temperature. Results are shown in Fig. 6.

As shown in Fig. 6, the *DEs* of MET and CIP using the various catalysts are ordered as follows: MBC-Air > MBC-N_2 > BC-Air-pH 10 > BC-N_2-pH 10 > BC-Air > BC-N_2 > TSS_0. The sonocatalytic degradation of MET and CIP using different materials are well described by pseudo-first-order kinetics (R^2: 0.9524–0.9965), and the k_1 values for MET and CIP degradation are 0.053, 0.047, 0.041, 0.039, 0.034, 0.031, 0.022 min^{-1}; and 0.045, 0.041, 0.037, 0.035, 0.031, 0.028, 0.018 min^{-1} with the US/MBC-Air, US/MBC-N_2, US/BC-Air-pH 10, US/BC-N_2-pH 10, US/BC-Air, US/BC-N_2, and US/TSS_0 processes, respectively. The relevant *SE* values of the various US/catalysts processes for MET and CIP removal were calculated to be 0.76, 1.07, 1.17, 1.34, 1.41, 1.62, 1.83 and 0.75, 1.17, 1.29, 1.46, 1.54, 1.71, 1.88 (Table S6). MBC-Air was thus selected as the optimal catalyst from among the various materials. Compared with sonication alone, the addition of TSS_0 to the sonolytic systems inhibited the degradation of MET and CIP, resulting in a 24% and 25% reduction in k_1 values, respectively. The results can be attributed to the competitive reaction of ROS with components of TSS_0, instead of MET or CIP.

To investigate the effect of catalyst dose, 50 mL of 30.2 μM MET solution was sonicated at 500 kHz and 259 W with 5–25 mg MBC-Air. The results are shown in Figs. 6c and 5d. As shown, the higher dose of MBC-Air leads to faster MET and CIP degradation. Similar results regarding the sonocatalytic degradation of MET and oxytetracycline were reported by Sheikhmohammadi *et al.*, and Hassandoost *et al.*, respectively [18,73]. High R^2 values (0.9594–0.9965) prove that the sonocatalytic degradation of MET and CIP is well described by pseudo-first-order kinetics. When increasing the MBC-Air dose from 0.1 to 0.5 g L^{-1}, the k_1 values increase from 0.053 to 0.086 min^{-1} for MET and from 0.045 to 0.076 min^{-1} for CIP (Table S7), resulting in an increase in the k_1 values by 62.3% for MET and 68.9% for CIP. The accelerated degradation may arise from (i) the higher catalyst dose providing more nuclei for the generation of cavities and more active sites for adsorption, followed by more intensified *in-situ* oxidizing of MET and CIP over the MBC-Air surface; (ii) the presence of Fe and causing the improved generation of ROS, H_2O_2 and e^-/h^+ pairs in sonocatalytic systems (Reactions 1–22) [20].

3.5. Effects of critical factors on the sonocatalytic degradation of MET

Ultrasonic frequency and power, initial concentration, reaction volume, and bulk temperature can affect the sonocatalytic degradation kinetics of ABX in aqueous solutions to different degrees [14].

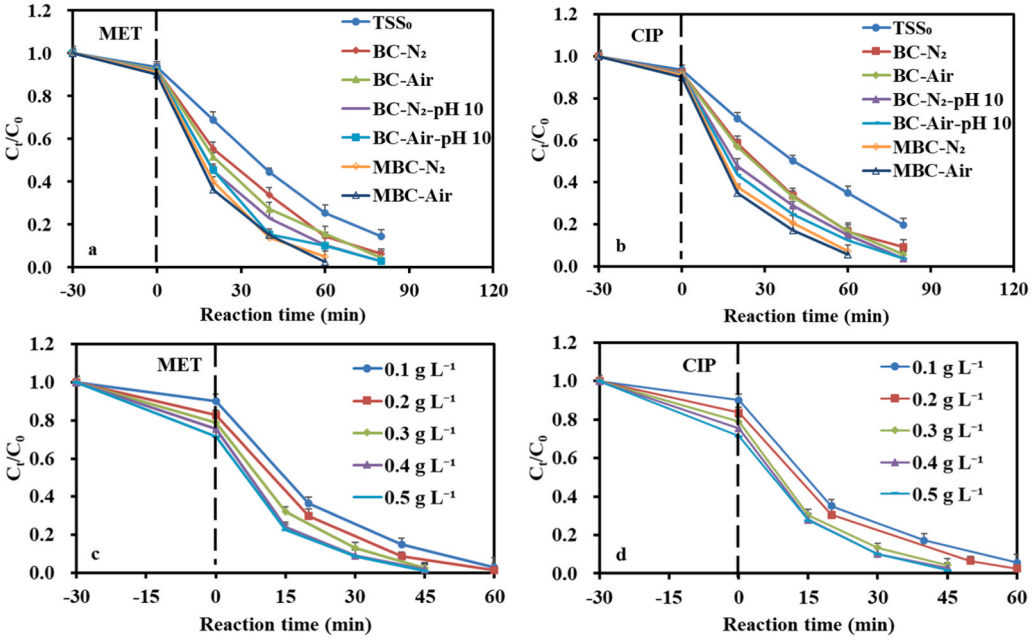

Fig. 6. Effects of catalyst type (a, b) and dose (c, d) on the sonocatalytic degradation of MET and CIP (conditions: initial MET or CIP concentration before adsorption, 30.2 μM; reaction volume, 50 mL; US frequency, 500 kHz; US power, 259 W; pH 7; room temperature).

3.5.1. Effect of ultrasonic frequency and power

In sonication-induced sonoluminescence processes, lower ultrasonic frequencies can enhance photon energy, while higher ultrasonic frequencies favor an intensification in photon numbers [74]. To investigate the effect of ultrasonic frequency, 50 mL of 30.2 μM MET solution was sonicated at 40, 80, 120, and 500 kHz in a comparable power range of 71–87 W with 5 mg MBC-Air at room temperature and pH 7. The results are presented in Table S8. As shown, the k_1 values of MET degradation positively correlate with the ultrasonic frequencies, and the degradation follows pseudo-first-order kinetics well (R^2: 0.9913–0.9969). Upon increasing ultrasonic frequencies from 40 to 120 kHz, the k_1 values increase by 90.0%, while the k_1 value at 500 kHz is 2.8 times higher than that at 40 kHz. Similar results regarding the sonocatalytic degradation of CIP and atrazine have been reported by Fan *et al.*, and Dehvari *et al.*, respectively [75,76]. The promoted degradation of MET may be attributed to: i) a higher number of smaller microbubbles being generated at higher ultrasonic frequencies followed by intensified cavitation effects and the enhanced formation of $^{\bullet}$OH radicals; ii) the higher ultrasonic frequencies promoting the mass transfer of MET and $^{\bullet}$OH radicals, and improving the dispersion of microbubbles and MBC-Air in sonocatalysis; iii) the higher ultrasonic frequencies creating higher accessibility to active sites by more effectively cleaning the surface of MBC-Air [14,75].

Ultrasonic power affects the degradation of ABX by changing the intensity of acoustic cavitation [20]. To investigate the effect of ultrasonic power, 50 mL of 30.2 μM MET solution was sonicated at 500 kHz and 73, 113, 129, 207, 259 W with 5 mg MBC-Air at room temperature and pH 7. The results are shown in Table S9. As shown, the k_1 values of MET degradation increase with increasing ultrasonic power. The sonocatalytic degradation of MET at various ultrasonic powers follows pseudo-first-order kinetics (R^2: 0.9508–0.9937). Upon increasing ultrasonic power from 73 to 259 W, the k_1 values increase by 89.3%. Sheikhmohammadi *et al.,* and Hassandoost *et al.,* have reported similar results in the sonocatalytic degradation of MET and oxytetracycline, respectively [18,73]. The promoted degradation of MET at higher ultrasonic powers may be the result of the higher input energy, higher number of cavitation events, intensified cavitation effects, and the enhanced generation of ROS and H_2O_2. In addition, the stronger micro-jets/turbulence triggered by higher powers could also lead to better mass transfer and cleaning of the MBC-Air surfaces in sonocatalytic systems [18,73].

3.5.2. Effect of initial concentration and reaction volume

The investigation of sonocatalytic kinetics at various initial concentrations is of great practical significance as the residual concentrations of ABX in effluents are generally variable. To investigate the effect of initial ABX concentration, 50 mL of 7.5, 15.1, and 30.2 μM MET (*i.e.* 1.29, 2.59, and 5.17 mg L^{-1} MET) solutions were sonicated at 500 kHz and 259 W with 5 mg MBC-Air at room temperature and pH 7. The results are shown in Table S10. The k_1 values of pseudo-first-order kinetics increased by 45.2% when initial MET concentrations were reduced from 30.2 to 7.5 μM (Table S10). Similarly, Sheikhmohammadi *et al.,* and Afzal *et al.,* have also reported that *DEs* decrease with increasing initial MET and CIP concentrations [18,77]. The limited degradation that occurs at higher initial MET concentrations may arise from: i) there being adequate ROS for removing smaller amounts of MET at lower initial concentrations; ii) the greater consumption of ROS by intermediates; iii) the reduced formation of cavities and ROS due to the increasing amounts of MET occupying more active sites over the surface of MBC-Air [14,20,73].

The investigation of sonocatalytic kinetics at various reaction volumes also favors the evaluation of treatment capabilities, allowing optimize the ultrasonic systems and identify the ABX removal mechanism at work. In order to investigate the effect of reaction volume, 50–250 mL of 30.2 μM MET solution was sonicated at 500 kHz and 259 W with 5 mg MBC-Air at room temperature and pH 7. The results are shown in Table S10. As shown, the k_1 values of pseudo-first-order kinetics decrease by 37.7% when reaction volumes are increased from 50 to 250 mL. The slower degradation of MET when using large reaction volumes may be related to the increasing number of dead zones, the higher recombination of ROS, *e.g.* $^{\bullet}$OH, $O_2^{\bullet-}$, $HO_2^{\bullet}$, *etc.* (Reactions 11–13) and e^-/h^+ pairs, and higher consumption of ROS by H_2O_2 and $^{\bullet}$H (Reactions 14 and 19) in sonocatalytic systems.

3.5.3. Effect of bulk temperature

To investigate the effect of bulk temperature, 50 mL of a 30.2 μM MET solution was sonicated at 500 kHz, 259 W, and pH 7 with 5 mg MBC-Air at 12, 25, and 38 °C. The result is shown in Table S11. As shown, the k_1 values of pseudo-first-order kinetics increase by 16.7% when the bulk temperatures increase from 12 to 38 °C. The apparent activation energy (E_a, J mol^{-1}) facilitates the elaboration of the temperature dependence of ABX removal, which can be calculated using the Arrhenius equation [72,78]. The low E_a value (4.4 kJ mol^{-1}) suggests that the sonocatalytic degradation of MET in aqueous solutions required very low activation energy and could be easily achieved, as well as indicating that the degradation of MET is diffusion-controlled. Dehvari *et al.*, have also reported a low E_a value (11.7 kJ mol^{-1}) being observed during the sonocatalytic degradation of atrazine [75].

3.6. Proposed sonocatalytic mechanism

To further elucidate the sonocatalytic mechanisms at work, the removal of MET and CIP were compared. 50 mL of 30.2 μM MET and CIP solutions were sonicated at 500 kHz and 259 W with 5 mg MBC-Air at room temperature and pH 7. The results are shown in Fig. 7.

As shown in Fig. 7, the sonolytic degradation of MET is faster than that of CIP, regardless of the use of MBC-Air, while degradation was accelerated for both in the presence of MBC-Air. The k_1 values for the sonolytic and sonocatalytic degradation of MET and CIP are 0.029 and 0.053 min^{-1}, as well as 0.024 and 0.045 min^{-1}, respectively. The *SE* values were calculated to be 1.83 and 1.88 for MET and CIP, respectively, leading to *DEs* of 96.9% and 93.7% and residual concentrations of 143.9 and 294.1 μg L^{-1}, after sonocatalytic degradation. A great amount of cavities is generated during sonication and three reaction zones are thus created; inside cavities, at the gas/liquid cavity interface, and in the bulk liquid [14]. Abundant $^{\bullet}$OH can be generated at the gas/liquid cavity interface during cavity collapse. As shown in Table S1, MET possesses a higher $LogK_{OW}$ value (-0.02) than CIP (-0.33), indicating that MET has higher hydrophobicity than CIP. Compared with CIP, MET possesses a smaller molecule size and higher solubility in water (Table S1). These features may result in MET displaying faster degradation than CIP in sonolytic and sonocatalytic systems; high

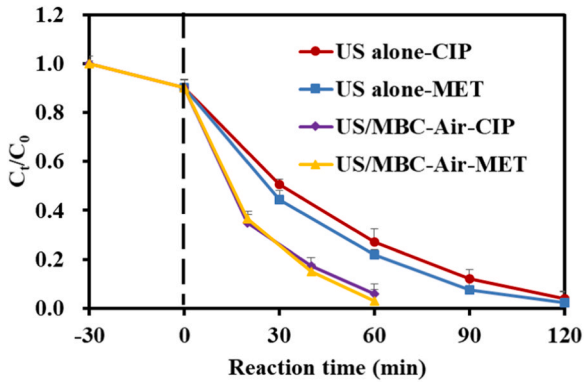

Fig. 7. Comparison of the sonocatalytic degradation of MET and CIP (conditions: initial ABX concentration before treatment, 30.2 μM; reaction volume, 50 mL; dosage of MBC-Air, 0.1 g L^{-1}; US frequency, 500 kHz; US power, 259 W; pH 7; room temperature).

hydrophobicity, small molecule size, and good solubility favor the mass transfer of MET to the gas/liquid cavity interface, where •OH radicals are abundant.

To investigate the role of •OH, *n*-butanol was added to the US/MBC-Air systems to act as a radical scavenger. 50 mL of 30.2 μM MET and CIP solutions was sonicated at 500 kHz and 259 W with 5 mg MBC-Air and 50 mM *n*-butanol at room temperature and pH 7. The k_1 values of MET and CIP degradation via sonocatalysis with MBC-Air and added *n*-butanol are 0.030 and 0.022 min^{-1}, respectively. The efficiencies of the inhibition of the k_1 values by *n*-butanol are 43.4% for MET and 51.1% for CIP, illustrating that •OH-based oxidation is of great importance during sonocatalysis with MBC-Air. The reaction rates of *n*-butanol and the model ABX with •OH are ordered as CIP (6.2×10^9 M^{-1} s^{-1}) > MET (5.0×10^9 M^{-1} s^{-1}) > *n*-butanol (5.5×10^8 M^{-1} s^{-1}), which reveals that the reaction rates with •OH radicals are not a determining factor for removing MET and CIP in sonocatalysis [79,80]. Although the *n*-butanol scavenger can rapidly capture •OH radicals during sonocatalysis, the concentration of •OH radicals at the gas/liquid interfacial is much higher than that in the bulk liquid [79]. Thus, the more hydrophobic MET can react with more •OH radicals than the relatively hydrophilic CIP. These results indicate that the hydrophobicity of ABX controls the sonocatalytic degradation kinetics of MET and CIP by determining their reaction zone.

To better understand the role of •OH radicals, sonocatalytic degradation was conducted with the addition of H_2O_2. 50 mL of 30.2 μM MET and CIP solutions was sonicated at 500 kHz and 259 W with 5 mg MBC-Air and 0.5–2.0 mM H_2O_2 at room temperature and pH 7 for 60 min. The results are shown in Fig. 8.

As shown in Fig. 8, the addition of H_2O_2 slightly accelerates the sonocatalytic degradation of MET and CIP, with a higher dose of H_2O_2 leading to faster degradation. The degradation of MET and CIP follows pseudo-first-order kinetics (R^2: 0.9664–0.9992). With the addition of 0.5, 1.0 and 2.0 mM H_2O_2, the k_1 values are 0.054, 0.056, 0.058 min^{-1} for MET and 0.047, 0.049, 0.050 min^{-1} for CIP, resulting in *DEs* and residual concentrations of 97.1%, 97.2%, 97.7% and 136.2, 129.4, 108.2 μg L^{-1} for MET, and 94.9%, 95.2%, 95.2% and 237.6, 225.9, 224.3 μg L^{-1} for CIP after 60 min of treatment. Upon increasing the dose of H_2O_2 from 0.5 to 2.0 mM, the k_1 value enhancement efficiencies increased from 1.9% to 9.4% for MET and 4.4%–11.1% for CIP. These results may be caused by the increased generation of •OH radicals via the Fenton-like process, and the reduction of H_2O_2 in the conduction band, *etc.* (Reactions 15–22) [20]. Overall, •OH radicals are crucial to the sonocatalytic degradation of the model ABX.

Based on the above discussion, the sonocatalytic mechanisms for the removal of the model ABX are proposed in Fig. 9.

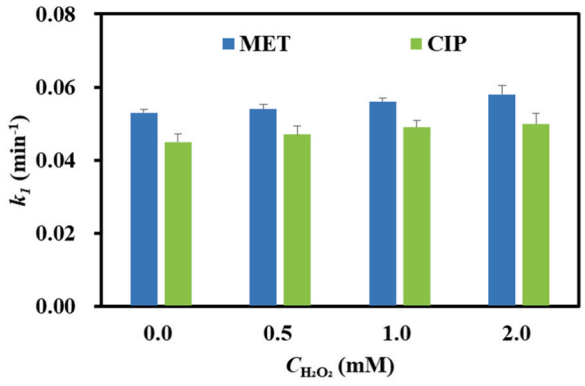

Fig. 8. Effect of adding H_2O_2 to the sonocatalytic degradation of MET and CIP (conditions: initial ABX concentration before treatment, 30.2 μM; reaction volume, 50 mL; reaction time, 60 min; dose of MBC-Air, 0.1 g L^{-1}; US frequency, 500 kHz; US power, 259 W; pH 7; room temperature).

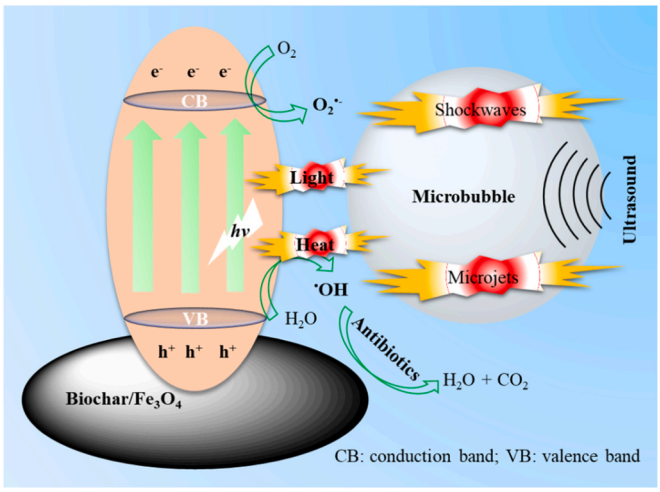

Fig. 9. The proposed sonocatalytic mechanisms for model ABX removal.

3.7. Intermediates and pathways of sonocatalytic degradation of MET and CIP

The identification of the intermediates from the model ABX facilitates the identification of the removal mechanisms and the deconstruction of the degradation pathways. To determine the major by-products of the model ABX, the sonocatalytic degradation of MET and CIP was performed at a higher initial concentration. 50 mL of 151 μM MET and CIP aqueous solutions was sonicated at 500 kHz and 259 W for 3 h with the addition of 5 mg MBC-Air at room temperature. The by-products were analyzed using the UPLC-MS/MS method as shown in Section 2.4. The chromatograms obtained from LC-MS/MS in positive-ionization mode for the model ABX and their intermediates are shown in Fig. S4. The associated k_1 values were 0.042 and 0.034 min^{-1} for MET and CIP, respectively, leading to *DEs* of 99.8% and 99.9%, and residual concentrations of 46.2 and 60.0 μg L^{-1}.

For MET, the peak of the parent compound, with an *RT* value of 9.10 min, was confirmed by the molecular ion of $[M + H]^+$ at *m/z* 171.811. The main fragment ions of the protonated molecular ion ($[M + H]^+$) of MET included *m/z* 114.499 (*RT*: 8.28 min), *m/z* 103.361 (*RT*: 2.07 min), *m/z* 102.416 (*RT*: 2.28 min), *m/z* 85.269 (*RT*: 7.56 min) and *m/z* 82.231 (*RT*: 3.03 min). MET underwent dehydroxyethylation, denitration, and electrophilic additions on the imidazole ring to produce *m/z* 85 (a) and (b) with isomeric structures [81]. The *m/z* 114 peak may be formed via the demethylation and dehydroxyethylation of MET molecules [81]. The fragment ions *m/z* 102, and *m/z* 103, and their isomeric structures may be directly derived from MET molecules via various pathways. MET underwent the ring-opening of the imidazole, denitration, demethylation, hydroxylation, dehydroxyethylation, and the loss of ethanolamine to generate *m/z* 102 (a) and *m/z* 103 (b) [81]. Intermediates *m/z* 103 (a) and *m/z* 102 (b) directly stemmed from the MET molhydroxymethylationecule via the ring-opening of imidazole, denitration, and/or carbonylation [82]. The smaller fragment ion *m/z* 82 may be produced via the complex pyrrolidization, demethylation, denitration and dehydroxyethylation of MET molecules. From the above-described results, the sonocatalytic degradation pathways of MET are proposed in Fig. 10.

For CIP, the peak of the parent compound, with an *RT* value of 11.94 min, was confirmed by the molecular ion of $[M + H]^+$ at *m/z* 332.063. The principal fragment ions of the protonated molecular ion ($[M + H]^+$) included *m/z* 348.061 (*RT*: 12.12 min), *m/z* 330.038 (*RT*: 11.32 min), *m/z* 306.075 (*RT*: 11.63 min), *m/z* 304.05 (*RT*: 10.96 min), *m/z* 262.941 (*RT*: 13.58 min), *m/z* 86.282 (*RT*: 1.96 min) and *m/z* 57.062 (*RT*: 2.14 min). CIP underwent the electrophilic substitutions of -OH on the N-containing six-membered ring and the benzene ring to

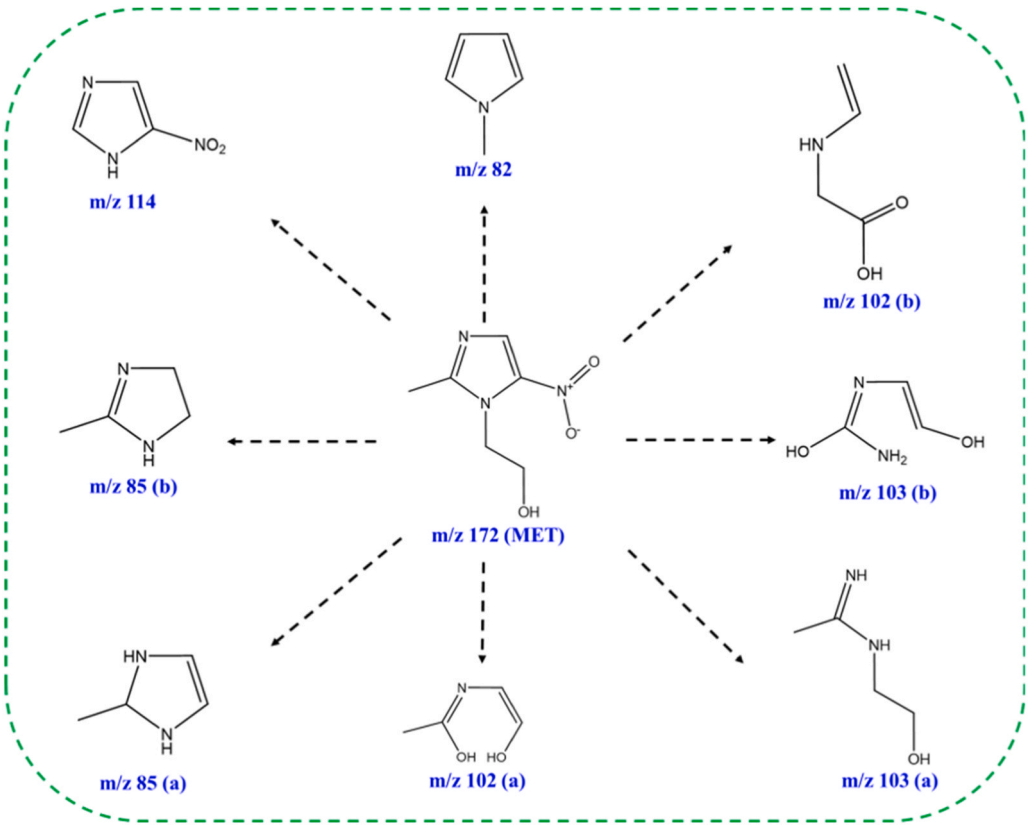

Fig. 10. The proposed pathways of the sonocatalytic degradation of MET in aqueous solution.

produce *m/z* 348 and *m/z* 330 (a) [76], respectively. Afterward, *m/z* 348 and *m/z* 330 (a) underwent decarboxylation, the opening of the N-containing six-membered ring, carboxylation, carbonylation, and hydroxylation to form *m/z* 306 (a) [76]. A series of intermediates are derived from *m/z* 348 via, sequentially, hydrogen abstraction (*m/z* 330 (b)), the opening of the piperazine ring (*m/z* 306 (b)), hydrogen abstraction (*m/z* 304 (a) and (b)), and the cleavage of N-containing side chain (*m/z* 263) [83–85]. Furthermore, more violent oxidation directly or indirectly led to the generation of smaller-size intermediates *m/z* 86 and *m/z* 57 down to inorganic H_2O and CO_2 [86,87]. From the

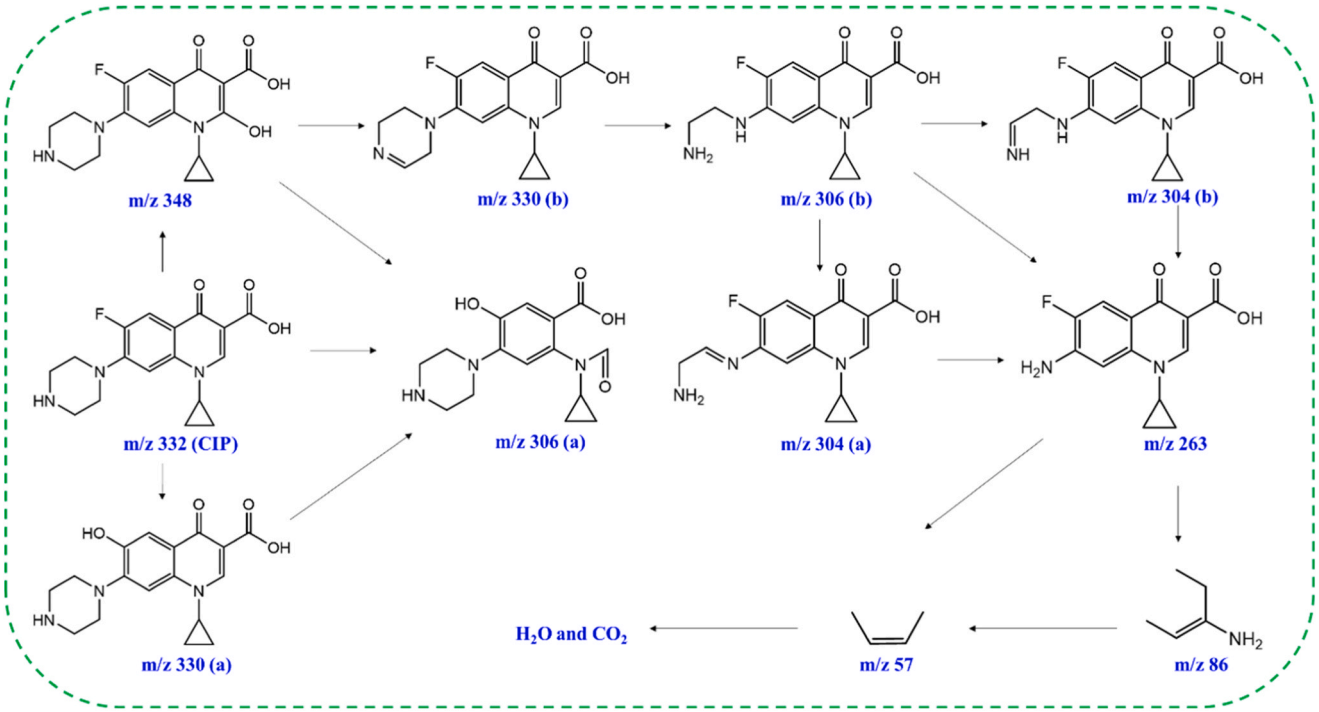

Fig. 11. The proposed pathways of the sonocatalytic degradation of CIP in aqueous solution.

above-described results, the sonocatalytic degradation pathways of CIP are shown in Fig. 11.

Intermediates of MET and CIP with lower molecular weight suggest that MET and CIP both were degraded, and the model ABX were possible to be decomposed into inorganics H_2O and CO_2. Nevertheless, the as-formed intermediates may affect microbial communities or contribute to resistance [88–90]. For instance, the antibacterial activity of CIP solutions decreased after sonocatalytic degradation using $BiOBr/BiFeO_3$. The average numbers of colonies after culture without adding solutions, and adding CIP solutions before and after sonication were 1656, 78, and 1253, respectively [91]. The toxicity of the CIP solution is reduced after sonophotocatalytic degradation, only one case of *Daphnia magna* disappeared after 2 days [92]. The toxicity of CIP solutions was reduced after photocatalytic degradation. After 2 days, the half-maximal effective concentration values of CIP solutions before and after treatment were 51.3 and 144.2, respectively [93]. 10 mg L^{-1} MET has no inhibition effect/acute toxicity towards *V. fischeri* [94]. The mechanisms of MET resistance are complex, which was first described in a clinical isolate of *B. fragilis* in 1978 [95]. The intermediates exhibit lower bioconcentration factors than MET, which are lower than that of MET with more than half of them assessed as mutagenic negative, and only five intermediates have higher acute toxicity than MET. The toxicity risk of the intermediates is remarkably reduced, yet, the majority of intermediates exhibited a higher potential for developmental toxicity than MET. Raw MET solution posed ab. 21.91% inhibition to *E. coli.*, whereas the toxicity of the treated solution via the UV/chlorine was insignificant, indicating chlorine photolysis does not have a substantial effect on the toxicity of the intermediates. The toxicity of the intermediates in UV/chlorine/TiO_2 rose in the earlier stage while decreasing with further treatment [96]. All the intermediates have lower toxicity than the initial MET. The Lethal Concentration 50, half-maximal effective concentration, and chronic values of all the intermediates including short-chain carboxylic acids were higher than those of MET. All the intermediates were free of acute toxicity, whereas only one product was harmful regarding chronic toxicity under solar radiation [97]. MET is a typical mutagenic contaminant. The mutagenicity of all the intermediates was lower than MET. The SnZVI/PS process effectively reduced the ecological toxicity of MET [98].

4. Conclusions

Herein, BCs and MBCs have been successfully fabricated via the MW-assisted hydrothermal treatment of OMWW without/with $FeCl_2{\cdot}4H_2O$ and $FeCl_3{\cdot}6H_2O$ under a N_2 or air atmosphere for the sonocatalytic degradation of MET and CIP in aqueous solutions. After the preparation of MBCs, the quality of OMWW improved to a certain degree. The prepared BCs and MBCs were characterized by N_2 physisorption at low temperatures, FESEM combined with EDS, PXRD, TGA, and FT-IR, and the results show that MBC-Air possesses better physicochemical properties than the other materials obtained. MBC-Air displays better adsorption and degradation performance than the other materials and can easily be separated from reaction systems. The main mechanism for the sonocatalytic degradation of MET and CIP focuses on their hydrophobic properties, and hydrophobic MET is more easily degraded than hydrophilic CIP. Adding H_2O_2 and high doses of MBC-Air facilitate the degradation of ABX due to the additional $^{\bullet}OH$ formation and more abundant activation sites over biochar. Quenching tests revealed that $^{\bullet}OH$ radicals are crucial for oxidizing MET and CIP in sonocatalysis. This work provides a reference for the preparation of catalysts and the purification of components in water matrices.

The advantages of prepared biochar are the economical synthesis and the convenience of separation, while the main drawback is the low catalytic efficiency, which is associated with a long treatment time (up to 1 h). In order to reduce energy consumption, rapid hydrothermal synthesis with MW was used instead of conventional hydrothermal synthesis. Thus, the MW-assisted hydrothermal process for biochar production in its current form is probably feasible on a large scale. On the other hand, it is generally recognised that scaling up the simple ultrasonic degradation process is quite difficult, while scaling up sonocatalytic degradation is possible. As for the potential environmental impact of using magnetic biochar, not only the environmental burden from the OMWW can be reduced, but the environmental risks from the spread of ABX can also be eliminated. Overall, the use of magnetic biochar has a positive impact on the environment. In terms of the overall sustainability of the process, the current study follows the principles of circular economy, whereby oil mill wastewater was treated in a MW-assisted hydrothermal process and with simultaneously produced magnetic biochar, which was used as a catalyst for the sonocatalytic degradation of MET and CIP in aqueous solutions.

In the future, life cycle analysis (LCA) can be used to assess the potential environmental impact of synthetic magnetic biochar. First, the system boundaries from raw material acquisition (biomass and magnetic material source and transportation) to synthesis processes (pretreatment, magnetization, carbonization) to downstream processing are clarified. Secondly, an analysis list covering raw materials (biomass and magnetic material-related parameters), energy consumption (type and quantity of energy in each link), and waste emissions (gas, liquid, solid waste) should be presented. In the impact assessment, the environmental impact is characterized and quantified after classification, and the overall impact is optionally weighted to be assessed. In the analysis of the results, the key environmental impact factors such as the use of chemical reagents and energy consumption in the synthesis process are analyzed. At the same time, some suggestions were put forward to optimize the synthesis process to reduce energy consumption, adopt environmentally friendly magnetic material sources, and further improve wastewater treatment. Finally, the environmental advantages and disadvantages compared with other materials or processes can be further clarified, which can provide a reference for the sustainable development of magnetic biochar.

CRediT authorship contribution statement

Maela Manzoli: Writing – original draft, Supervision, Formal analysis, Data curation. **Giancarlo Cravotto:** Writing – review & editing, Supervision, Project administration, Conceptualization. **Pengyun Liu:** Writing – original draft, Investigation, Formal analysis. **Zhilin Wu:** Writing – original draft, Methodology, Data curation, Conceptualization.

Declaration of Competing Interest

The authors declare that they have no known competing financial interests or personal relationships that could have appeared to influence the work reported in this paper.

Acknowledgments

This research was supported by both the University of Turin (Ricerca locale 2023) and the China Scholarship Council (CSC). Liu P. acknowledges the support of the CSC (grant No. 201909505008). The authors are grateful to Mr. Stefano Mantegna, Dr. Giorgio Grillo, Dr. Marco Belluati, Dr. Manuel Salgado-Ramos, Dr. Fabio Bucciol, Dr. Lorenzo Gallina, Dr. Federico Verdini and Dr. Luisa Boffa for technical assistance.

Appendix A. Supporting information

Supplementary data associated with this article can be found in the online version at doi:10.1016/j.jece.2024.114996.

Data availability

No data was used for the research described in the article.

References

[1] R. Gothwal, T. Shashidhar, Antibiotic pollution in the environment: a review, Clean. -Soil, Air, Water 43 (2015) 479–489, https://doi.org/10.1002/clen.201300989.

[2] P. Grenni, V. Ancona, A.B. Caracciolo, Ecological effects of antibiotics on natural ecosystems: A review, Microchem. J. 136 (2018) 25–39, https://doi.org/10.1016/j.microc.2017.02.006.

[3] M. Bilal, S. Mehmood, T. Rasheed, H.M. Iqbal, Antibiotics traces in the aquatic environment: persistence and adverse environmental impact, Curr. Opin. Environ. Sci. Health 13 (2020) 68–74, https://doi.org/10.1016/j.coesh.2019.11.005.

[4] M.S. Mohsenzadeh, A. Mohammadinejad, S.A. Mohajeri, Simple and selective analysis of different antibiotics in milk using molecularly imprinted polymers: a review, Food Addit. Contam. A. 35 (2018) 1959–1974, https://doi.org/10.1080/19440049.2018.1508889.

[5] S.A. Khatibi, S. Hamidi, M.R. Siahi-Shadbad, Current trends in sample preparation by solid-phase extraction techniques for the determination of antibiotic residues in foodstuffs: a review, Crit. Rev. Food Sci. 61 (2021) 3361–3382, https://doi.org/10.1080/10408398.2020.1798349.

[6] X. Zhang, M. Kamali, Y. Xue, S. Li, M.E.V. Costa, D. Cabooter, R. Dewil, Periodate activation with copper oxide nanomaterials for the degradation of ciprofloxacin-A new insight into the efficiency and mechanisms, J. Clean. Prod. 383 (2023) 135412, https://doi.org/10.1016/j.jclepro.2022.135412.

[7] S. Pan, T. Zhao, H. Liu, X. Li, M. Zhao, D. Yuan, T. Jiao, Q. Zhang, S. Tang, Enhancing ferric ion/sodium percarbonate Fenton-like reaction with tungsten disulfide cocatalyst for metronidazole decomposition over wide pH range, Chem. Eng. J. 452 (2023) 139245, https://doi.org/10.1016/j.cej.2022.139245.

[8] X. Ma, C. He, Y. Yan, J. Chen, H. Feng, J. Hu, H. Zhu, Y. Xia, Energy-efficient electrochemical degradation of ciprofloxacin by a Ti-foam/PbO_2-GN composite electrode: Electrode characteristics, parameter optimization, and reaction mechanism, Chemosphere 315 (2023) 137739, https://doi.org/10.1016/j.chemosphere.2023.137739.

[9] S. Meini, C. Zini, M.T. Passaleva, A. Frullini, F. Fusco, R. Carpi, F. Piani, Pneumatosis intestinalis in COVID-19, BMJ Open Gastroenter 7 (2020) e000434, https://doi.org/10.1136/bmjgast-2020-000434.

[10] A.I. Wegbom, C.K. Edet, O. Raimi, A.F. Fagbamigbe, V.A. Kiri, Self-medication practices and associated factors in the prevention and/or treatment of COVID-19 virus: a population-based survey in Nigeria, Front. Public Health 9 (2021) 606801, https://doi.org/10.3389/fpubh.2021.606801.

[11] M. Wagil, J. Maszkowska, A. Bialk-Bieliska, M. Caban, P. Stepnowski, J. Kumirska, Determination of metronidazole residues in water, sediment and fish tissue samples, Chemosphere 119 (2015) S28–S34, https://doi.org/10.1016/j.chemosphere.2013.12.061.

[12] O. Ayanda, M. Amoo, O. Aremu, O. Oketayo, S. Nelana, Ultrasonic Degradation of Ciprofloxacin in the presence of Zinc Oxide Nanoparticles and Zinc Oxide/Acha Waste Composite, Res. J. Chem. Environ. 27 (2023) 22–28, https://doi.org/10.25303/2701rjce022028.

[13] Y.M. Hunge, A. Yadav, S.W. Kang, S.J. Lim, H. Kim, Visible light activated MoS_2/ZnO composites for photocatalytic degradation of ciprofloxacin antibiotic and hydrogen production, J. Photoch. Photobio. A. 434 (2023) 114250, https://doi.org/10.1016/j.jphotochem.2022.114250.

[14] P. Liu, Z. Wu, A.V. Abramova, G. Cravotto, Sonochemical processes for the degradation of antibiotics in aqueous solutions: A review, Ultrason. Sonochem. 74 (2021) 105566, https://doi.org/10.1016/j.ultsonch.2021.105566.

[15] A. Nasiri, F. Tamaddon, M.H. Mosslemin, M.A. Gharaghani, A. Asadipour, Magnetic nano-biocomposite $CuFe_2O_4$@ methylcellulose (MC) prepared as a new nano-photocatalyst for degradation of ciprofloxacin from aqueous solution, Environ. Health Eng. Manag. J. 6 (2019) 41–51, https://doi.org/10.15171/EHEM.2019.05.

[16] V. Homem, S. Lúcia, Degradation and removal methods of antibiotics from aqueous matrices–a review, J. Environ. Manag. 92 (2011) 2304–2347, https://doi.org/10.1016/j.jenvman.2011.05.023.

[17] P. Liu, Z. Wu, F.T. Cannizzo, S. Mantegna, G. Cravotto, Removal of antibiotics from milk via ozonation in a vortex reactor, J. Hazard. Mater. 440 (2022) 129642, https://doi.org/10.1016/j.jhazmat.2022.129642.

[18] A. Sheikhmohammadi, E. Asgari, H. Nourmoradi, M.M. Fazli, M. Yeganeh, Ultrasound-assisted decomposition of metronidazole by synthesized TiO_2/Fe_3O_4 nanocatalyst: Influencing factors and mechanisms, J. Environ. Chem. Eng. 9 (2021) 105844, https://doi.org/10.1016/j.jece.2021.105844.

[19] B. Kakavandi, N. Bahari, R.R. Kalantary, E. Dehghani, FardEnhanced sono-photocatalysis of tetracycline antibiotic using TiO_2 decorated on magnetic activated carbon (MAC@T) coupled with US and UV: A new hybrid system, Ultrason. Sonochem. 55 (2019) 75–85, https://doi.org/10.1016/j.ultsonch.2019.02.026.

[20] S. Dehghan, B. Kakavandi, R.R. Kalantary, Heterogeneous sonocatalytic degradation of amoxicillin using ZnO@Fe_3O_4 magnetic nanocomposite: influential factors, reusability and mechanisms, J. Mol. Liq. 264 (2018) 98–109, https://doi.org/10.1016/j.molliq.2018.05.020.

[21] K.S. Suslick, Sonochemistry, Science 247 (1990) 1439–1445, https://doi.org/10.1126/science.247.4949.1439.

[22] P. Kanthale, M. Ashokkumar, F. Grieser, Sonoluminescence, sonochemistry (H_2O_2 yield) and bubble dynamics: frequency and power effects, Ultrason. Sonochem. 15 (2008) 143–150, https://doi.org/10.1016/j.ultsonch.2007.03.003.

[23] P. Liu, Z. Wu, Lee, J.G. Cravotto, Sonocatalytic degrading antibiotics over activated carbon in cow milk, Food Chem. 432 (2024) 137168, https://doi.org/10.1016/j.foodchem.2023.137168.

[24] Z. Zarnegar, J. Safari, Heterogenization of an imidazolium ionic liquid based on magnetic carbon nanotubes as a novel organocatalyst for the synthesis of 2-amino-chromenes via a microwave-assisted multicomponent strategy, N. J. Chem. 40 (2016) 7986–7995, https://doi.org/10.1039/C6NJ01631F.

[25] Y. Wang, X. Zhu, D. Feng, A.K. Hodge, L. Hu, J. Lü, J. Li, Biochar-supported FeS/Fe_3O_4 composite for catalyzed fenton-type degradation of ciprofloxacin, Catalysts 9 (2019) 1062, https://doi.org/10.3390/catal9121062.

[26] J. Dong, W. Xu, S. Liu, Y. Gong, T. Yang, L. Du, Q. Chen, X. Tan, Y. Liu, Lignin-derived biochar to support $CoFe_2O_4$: Effective activation of peracetic acid for sulfamethoxazole degradation, Chem. Eng. J. 430 (2021) 132868, https://doi.org/10.1016/j.cej.2021.132868.

[27] A. Khataee, B. Kayan, P. Gholami, D. Kalderis, S. Akay, Sonocatalytic degradation of an anthraquinone dye using TiO_2-biochar nanocomposite, Ultrason. Sonochem. 39 (2017) 120–128, https://doi.org/10.1016/j.ultsonch.2017.04.018.

[28] A. Khataee, B. Kayan, P. Gholami, D. Kalderis, S. Akay, L. Dinpazhoh, Sonocatalytic degradation of Reactive Yellow 39 using synthesized ZrO_2 nanoparticles on biochar, Ultrason. Sonochem. 39 (2017) 540–549, https://doi.org/10.1016/j.ultsonch.2017.05.023.

[29] A. Khataee, P. Gholami, D. Kalderis, E. Pachatouridou, M. Konsolakis, Preparation of novel CeO_2-biochar nanocomposite for sonocatalytic degradation of a textile dye, Ultrason. Sonochem. 41 (2018) 503–513, https://doi.org/10.1016/j.ultsonch.2017.10.013.

[30] S. Li, Z. Wang, X. Zhao, X. Yang, G. Liang, X. Xie, Insight into enhanced carbamazepine photodegradation over biochar-based magnetic photocatalyst Fe_3O_4/BiOBr/BC under visible LED light irradiation, Chem. Eng. J. 360 (2019) 600–611, https://doi.org/10.1016/j.cej.2018.12.002.

[31] K. Talukdar, B.M. Jun, Y. Yoon, Y. Kim, A. Fayyaz, C.M. Park, Novel Z-scheme Ag_3PO_4/Fe_3O_4-activated biochar photocatalyst with enhanced visible-light catalytic performance toward degradation of bisphenol A, J. Hazard. Mater. 398 (2020) 123025, https://doi.org/10.1016/j.jhazmat.2020.123025.

[32] M. Hassan, R. Naidu, J. Du, Y. Liu, F. Qi, Critical review of magnetic biosorbents: Their preparation, application, and regeneration for wastewater treatment, Sci. Total Environ. 702 (2020) 134893, https://doi.org/10.1016/j.scitotenv.2019.134893.

[33] S. Chellappan, K. Aparna, C. Chingakham, V. Sajith, V. Nair, Microwave assisted biodiesel production using a novel Brønsted acid catalyst based on nanomagnetic biocomposite, Fuel 246 (2019) 268–276, https://doi.org/10.1016/j.fuel.2019.02.104.

[34] X.-S. Li, G.-T. Zhu, Y.-B. Luo, B.-F. Yuan, Y.-Q. Feng, Synthesis and applications of functionalized magnetic materials in sample preparation, TrAC Trend Anal. Chem. 45 (2013) 233–247, https://doi.org/10.1016/j.trac.2012.10.015.

[35] A. Nasiri, M. Malakootian, M.R. Heidari, S.N. Asadzadeh, $CoFe_2O_4$@ methylcelluloluse as a new magnetic nano biocomposite for sonocatalytic degradation of reactive blue 19, J. Polym. Environ. 29 (2021) 2660–2675, https://doi.org/10.1007/s10924-021-02074-w.

[36] S. Rajabi, A. Nasiri, M. Hashemi, Enhanced activation of persulfate by $CuCoFe_2O_4$@MC/AC as a novel nanomagnetic heterogeneous catalyst with ultrasonic for metronidazole degradation, Chemosphere 286 (2022) 131872, https://doi.org/10.1016/j.chemosphere.2021.131872.

[37] A. Hesham, Y. Awad, H. Jahin, S. El-Korashy, S. Maher, H. Kalil, G. Khairy, Hydrochar for industrial wastewater treatment: an overview on its advantages and applications, J. Environ. Anal. Toxicol. 11 (2021), https://doi.org/10.37421/2161-0525.21.11.626.

[38] S. Román, J. Libra, N. Berge, E. Sabio, K. Ro, L. Li, B. Ledesma, A. Álvarez, S. Bae, Hydrothermal carbonization: Modeling, final properties design and applications: A review, Energies 11 (2018) 216, https://doi.org/10.3390/en11010216.

[39] A.E. Nassar, I.E. Eslam, A.R. Sameh, E.G. Seleem, S.J. Hossam, Microwave-assisted hydrothermal preparation of magnetic hydrochar for the removal of organophosphorus insecticides from aqueous solutions, Sep. Purif. Technol. 306 (2023) 122569, https://doi.org/10.1016/j.seppur.2022.122569.

[40] S. Malghani, G. Gerd, E.T. Susan, Chars produced by slow pyrolysis and hydrothermal carbonization vary in carbon sequestration potential and greenhouse gases emissions, Soil Biol. Biochem. 62 (2013) 137–146, https://doi.org/10.1016/j.soilbio.2013.03.013.

[41] A. Khosravi, H. Zheng, Q. Liu, M. Hashemi, Y. Tang, B. Xing, Production and characterization of hydrochars and their application in soil improvement and environmental remediation, Chem. Eng. J. 430 (2022) 133142, https://doi.org/10.1016/j.cej.2021.133142.

[42] Y. Li, A. Meas, S. Shan, R. Yang, X. Gai, H. Wang, N. Tsend, Hydrochars from bamboo sawdust through acid assisted and two-stage hydrothermal carbonization for removal of two organics from aqueous solution, Bioresour. Technol. 261 (2018) 257–264, https://doi.org/10.1016/j.biortech.2018.03.108.

[43] H.B. Sharma, K.S. Ajitand, D. Brajesh, Hydrothermal carbonization of renewable waste biomass for solid biofuel production: A discussion on process mechanism, the influence of process parameters, environmental performance and fuel properties of hydrochar, Renewa. Sust. Energ. Rev. 123 (2020) 109761, https://doi.org/10.1016/j.rser.2020.109761.

[44] A. Kumar, S. Komal, B. Thallada, Hydochar and biochar: production, physicochemical properties and techno-economic analysis, Bioresour. Technol. 310 (2020) 123442, https://doi.org/10.1016/j.biortech.2020.123442.

[45] A. Khataee, B. Kayan, D. Kalderis, A. Karimi, S. Akay, M. Konsolakis, Ultrasound-assisted removal of Acid Red 17 using nanosized Fe_3O_4-loaded coffee waste hydrochar, Ultrason. Sonochem. 35 (2017) 72–80, https://doi.org/10.1016/j.ultsonch.2016.09.004.

[46] R. Li, Y. Zhang, H. Deng, Z. Zhang, J.J. Wang, S.M. Shaheen, R. Xiao, J. Rinklebe, B. Xi, X. He, J. Du, Removing tetracycline and Hg (II) with ball-milled magnetic

nanobiochar and its potential on polluted irrigation water reclamation, J. Hazard. Mater. 384 (2020) 121095, https://doi.org/10.1016/j.jhazmat.2019.121095.
[47] P. Liu, Z. Wu, X. Ge, X. Yang, Hydrothermal synthesis and microwave-assisted activation of starch-derived carbons as an effective adsorbent for naphthalene removal, RSC Adv. 9 (2019) 11696–11706, https://doi.org/10.1039/C9RA01386E.
[48] W. Li, Microwave-assisted hydrothermal synthesis and optical property of Co_3O_4 nanorods, Mater. Lett. 62 (2008) 4149–4151, https://doi.org/10.1016/j.matlet.2008.06.032.
[49] E.I. El-Aswar, S.E. Gaber, M.M. Zahran, A.H. Abdelaleem, Characterization of biosynthesized silver nanoparticles by Haplophyllum tuberculatum plant extract under microwave irradiation and detecting their antibacterial activity against some wastewater microbes, Desalin. Water Treat. 195 (2020) 275–285, https://doi.org/10.5004/dwt.2020.25876.
[50] L. Cao, I.K.M. Yu, D. Cho, D. Wang, D.C.W. Tsang, S. Zhang, S. Ding, L. Wang, Y. S. Ok, Microwave-assisted low-temperature hydrothermal treatment of red seaweed (Gracilaria lemaneiformis) for production of levulinic acid and algae hydrochar, Bioresour. Technol. 273 (2019) 251–258, https://doi.org/10.1016/j.biortech.2018.11.013.
[51] Z. Wu, P. Liu, Z. Wu, G. Cravotto, In situ modification of activated carbons by oleic acid under microwave heating to improve adsorptive removal of naphthalene in aqueous solutions, Processes 9 (2021) 391, https://doi.org/10.3390/pr9020391.
[52] L. Dai, C. He, Y. Wang, Y. Liu, Z. Yu, Y. Zhou, L. Fan, D. Duan, R. Ruan, Comparative study on microwave and conventional hydrothermal pretreatment of bamboo sawdust: Hydrochar properties and its pyrolysis behaviors, Energy Conv. Manag. 146 (2017) 1–7, https://doi.org/10.1016/j.enconman.2017.05.007.
[53] M. Bhattacharya, B. Tanmay, A review on the susceptor assisted microwave processing of materials, Energy 97 (2016) 306–338, https://doi.org/10.1016/j.energy.2015.11.034.
[54] H.M. Elshishini, G.M. Elsubruiti, Z.F. Ghatass, A.S. Eltaweil, Microwave-assisted synthesis of Zn–Fe LDH modified with magnetic oxidized hydrochar for Pb (II) removal: Insights into stability, performance and mechanism, J. Solid State Chem. 335 (2024) 124689, https://doi.org/10.1016/j.jssc.2024.124689.
[55] S.E. Elaigwu, M.G. Gillian, Microwave-assisted hydrothermal carbonization of rapeseed husk: a strategy for improving its solid fuel properties, Fuel Process. Technol. 149 (2016) 305–312, https://doi.org/10.1016/j.fuproc.2016.04.030.
[56] K. Ng, S. Weng, Adsorption of Trimethyltin, Arsenic (v), Zinc and Copper by Palm Oil Mill Sludge Biochar Prepared by Microwave, Diss. UTAR, 2016. http://eprints.utar.edu.my/id/eprint/2047.
[57] S. Nizamuddin, H.A. Baloch, M.T.H. Siddiqui, N.M. Mubarak, M.M. Tunio, A. W. Bhutto, A.S. Jatoi, G.J. Griffin, M.P. Srinivasan, An overview of microwave hydrothermal carbonization and microwave pyrolysis of biomass, Rev. Environ. Sci. Bio. 17 (2018) 813–837, https://doi.org/10.1007/s11157-018-9476-z.
[58] Y. Li, N. Tsend, T. Li, H. Liu, R. Yang, X. Gai, H. Wang, S. Shan, Microwave assisted hydrothermal preparation of rice straw hydrochars for adsorption of organics and heavy metals, Bioresour. Technol. 273 (2019) 136–143, https://doi.org/10.1016/j.biortech.2018.10.056.
[59] J. Qu, S. Wang, L. Jin, Y. Liu, R. Yin, Z. Jiang, Y. Tao, J. Huang, Y. Zhang, Magnetic porous biochar with high specific surface area derived from microwave-assisted hydrothermal and pyrolysis treatments of water hyacinth for Cr (VI) and tetracycline adsorption from water, Bioresour. Technol. 340 (2021) 125692, https://doi.org/10.1016/j.biortech.2021.125692.
[60] P. Liu, Z. Wu, Z. Fang, G. Cravotto, Sonolytic degradation kinetics and mechanisms of antibiotics in water and cow milk, Ultrason. Sonochem. 99 (2023) 106518, https://doi.org/10.1016/j.ultsonch.2023.106518.
[61] Y. Kitazono, I. Ihara, K. Toyoda, K. Umetsu, Antibiotic removal from waste milk by electrochemical process: degradation characteristics in concentrated organic solution, J. Mater. Cycles Waste Manag. 19 (2017) 1261–1269, https://doi.org/10.1007/s10163-016-0517-9.
[62] A. Esrafili, M. Tahergorabi, M. Malakootian, M. Kermani, M. Gholami, M. Farzadkia, Synergistic effects of catalytic and photocatalytic ozonation on four sulfonamides antibiotics degradation in an aquatic solution, Desalin. Water Treat. 182 (2020) 260–276, https://doi.org/10.5004/dwt.2020.25189.
[63] X. Ge, Z. W, G. Cravotto, M. Manzoli, P. Cintas, Z. Wu, Cork wastewater purification in a cooperative flocculation/adsorption process with microwave-regenerated activated carbon, J. Hazard. Mater. 360 (2018) 412–419, https://doi.org/10.1016/j.jhazmat.2018.08.022.
[64] R. Zhu, J. Xia, H. Zhang, F. Kong, X. Hu, Y. Shen, W.H. Zhang, Synthesis of magnetic activated carbons from black liquor lignin and Fenton sludge in a one-step pyrolysis for methylene blue adsorption, J. Environ. Chem. Eng. 9 (2021) 106538, https://doi.org/10.1016/j.jece.2021.106538.
[65] C. Gai, F. Zhang, Q. Lang, T. Liu, N. Peng, Z. Liu, Facile one-pot synthesis of iron nanoparticles immobilized into the porous hydrochar for catalytic decomposition of phenol, Appl. Catal. B: Environ. 204 (2017) 566–576, https://doi.org/10.1016/j.apcatb.2016.12.005.
[66] L. Kong, X. Lu, X. Bian, W. Zhang, C. Wang, Constructing carbon-coated Fe_3O_4 microspheres as antiacid and magnetic support for palladium nanoparticles for catalytic applications, ACS Appl. Mater. Interfaces 3 (2011) 35–42, https://doi.org/10.1021/am101077a.
[67] J. Sahari, S. Sapuan, E. Zainudin, M.A. Maleque, Mechanical and thermal properties of environmentally friendly composites derived from sugar palm tree, Mater. Des. 49 (2013) 285–289, https://doi.org/10.1016/j.matdes.2013.01.048.
[68] N.M. Nurazzi, M.R.M. Asyraf, M. Rayung, M.N.F. Norrrahim, S.S. Shazleen, M.S. A. Rani, A.R. Shafi, H.A. Aisyah, M.H.M. Radzi, F.A. Sabaruddin, R.A. Ilyas, E. S. Zainudin, K. Abdan, Thermogravimetric analysis properties of cellulosic natural fiber polymer composites: A review on influence of chemical treatments, Polymers 13 (2021) 2710, https://doi.org/10.3390/polym13162710.
[69] M.N. Norizan, K. Abdan, M.S. Salit, R. Mohamed, Physical, mechanical and thermal properties of sugar palm yarn fibre loading on reinforced unsaturated polyester composites, J. Phys. Sci. 28 (2017) 115–136, https://doi.org/10.21315/jps2017.28.3.8.
[70] P. Liu, Z. Wu, Z. Sun, J. Ye, Comparison study of naphthalene adsorption on activated carbons prepared from different raws, Korean J. Chem. Eng. 35 (2018) 2086–2096, https://doi.org/10.1007/s11814-018-0124-7.
[71] R.D.C. Soltani, M. Mashayekhi, M. Naderi, G. Boczkaj, S. SJorfi, M. afari, Sonocatalytic degradation of tetracycline antibiotic using zinc oxide nanostructures loaded on nano-cellulose from waste straw as nanosonocatalyst, Ultrason. Sonochem. 55 (2019) 117–124, https://doi.org/10.1016/j.ultsonch.2019.03.009.
[72] Y.A.J. Al-Hamadani, C. Jung, J.K. Im, L.K. Boateng, J.R.V. Flora, M. Jang, J. Heo, C.M. Park, Y. Yoon, Sonocatalytic degradation coupled with single-walled carbon nanotubes for removal of ibuprofen and sulfamethoxazole, Chem. Eng. Sci. 162 (2017) 300–308, https://doi.org/10.1016/j.ces.2017.01.011.
[73] R. Hassandoost, A. Kotb, Z. Movafagh, M. Esmat, R. Guegan, S. Endo, W. Jevasuwan, N. Fukata, Y. Sugahara, A. Khataee, Y. Yamauchi, Y. Ide, E. Doustkhah, Nanoarchitecturing bimetallic manganese cobaltite spinels for sonocatalytic degradation of oxytetracycline, Chem. Eng. J. 431 (2022) 133851, https://doi.org/10.1016/j.cej.2021.133851.
[74] M. Zhou, H. Yang, T. Xian, R. Li, H. Zhang, X. Wang, Sonocatalytic degradation of RhB over $LuFeO_3$ particles under ultrasonic irradiation, J. Hazard. Mater. 289 (2015) 149–157, https://doi.org/10.1016/j.jhazmat.2015.02.054.
[75] M. Dehvari, A.B. Ali, E. Shirin, Amplification of oxidative elimination of atrazine by Ultrasound/Ultraviolet–assisted Sono/Photocatalyst using a spinel cobalt ferrite–anchored MWCNT as peroxymonosulfate activator, J. Photochem. Photobiol. A: Chem. 437 (2023) 114452, https://doi.org/10.1016/j.jphotochem.2022.114452.
[76] G. Fan, C. Cai, S. Yang, B. Du, J. Luo, Y. Chen, X. Lin, Y. Wang, Sonophotocatalytic degradation of ciprofloxacin by $Bi_2MoO_6/FeVO_4$ heterojunction: Insights into performance, mechanism and pathway, Sep. Purif. Technol. 303 (2022) 122251, https://doi.org/10.1016/j.seppur.2022.122251.
[77] M.Z. Afzal, P. Zu, C.M. Zhang, J. Guan, C. Song, X.F. Sun, S.G. Wang, Sonocatalytic degradation of ciprofloxacin using hydrogel beads of TiO_2 incorporated biochar and chitosan, J. Hazard. Mater. 434 (2022) 128879, https://doi.org/10.1016/j.jhazmat.2022.128879.
[78] J. Sun, J. Feng, S. Shi, Y. Pi, M. Song, Y. Shi, Degradation of the antibiotic sulfamonomethoxine sodium in aqueous solution by photo-Fenton oxidation, Chin. Sci. Bull. 57 (2012) 558–564, https://doi.org/10.1007/s11434-011-4887-z.
[79] J. Hu, J. Wang, R. Chen, Degradation of 4-chlorophenol in aqueous solution by γ-radiation and ozone oxidation, Sci. China Ser. B. 49 (2006) 186–192, https://doi.org/10.1007/s11426-006-0186-y.
[80] S. Mandal, Reaction rate constants of hydroxyl radicals with micropollutants and their significance in advanced oxidation processes, J. Adv. Oxid. Technol. 21 (2018) 178–195, https://doi.org/10.26802/jaots.2017.0075.
[81] P. Song, Z. Yao, X. Zhang, Y. Liu, Y. Xu, J. Wang, In situ formation and activation of high-volume H_2O_2 in micro-nano dendritic ZVC/air system for enhanced Fenton-like degradation of metronidazole, J. Taiwan Inst. Chem. Eng. 142 (2023) 104639, https://doi.org/10.1016/j.jtice.2022.104639.
[82] M.L. Tran, C.H. Nguyen, C.C. Fu, R.S. Juang, Hybridizing Ag-Doped ZnO nanoparticles with graphite as potential photocatalysts for enhanced removal of metronidazole antibiotic from water, J. Environ. Manag. 252 (2019) 109611, https://doi.org/10.1016/j.jenvman.2019.109611.
[83] J. He, N. Li, D. Zhang, G. Zheng, H. Zhang, K. Yu, J. Jiang, Real-time monitoring of ciprofloxacin degradation in an electro-Fenton-like system using electrochemical-mass spectrometry, Environ. Sci: Water Res. Technol. 6 (2020) 181–188, https://doi.org/10.1039/C9EW00868C.
[84] T. An, H. Yang, G. Li, W. Song, W.J. Cooper, X. Nie, Kinetics and mechanism of advanced oxidation processes (AOPs) in degradation of ciprofloxacin in water, Appl. Catal. B: Environ. 94 (2010) 288–294, https://doi.org/10.1016/j.apcatb.2009.12.002.
[85] Y.C. Liu, J.Q. Wang, Y. Wang, C.L. Chen, X. Wang, Z. Xiang, Sonocatalytic degradation of ciprofloxacin by $BiOBr/BiFeO_3$, Appl. Catal. A-Gen. 643 (2022) 118776, https://doi.org/10.1016/j.apcata.2022.118776.
[86] D. Zheng, M. Wu, E. Zheng, Y. Wang, C. Feng, J. Zou, M. Juan, X. Bai, T. Wang, Y. Shi, Adsorption and oxidation of ciprofloxacin by a novel layered double hydroxides modified sludge biochar, J. Colloid Interf. Sci. 625 (2022) 596–605, https://doi.org/10.1016/j.jcis.2022.06.080.
[87] Y. Zhou, M. Yu, R. Zhan, X. Wang, G. Peng, J. Niu, Ti_3C_2 MXene-induced interface electron separation in $g\text{-}C_3N_4/Ti_3C_2$ MXene/$MoSe_2$ Z-scheme heterojunction for enhancing visible light-irradiated enoxacin degradation, Sep. Purif. Technol. 275 (2021) 119194, https://doi.org/10.1016/j.seppur.2021.119194.
[88] A. Sheikhmohammadi, E. Asgari, N. Alinejad, B. Hashemzadeh, Photocatalytic oxidation of ciprofloxacin by UV/α-Fe_2O_3/sulfite: mechanism, kinetic, degradation pathway, Intern. J. Environ. Health Res. 33 (2023) 192–205, https://doi.org/10.1080/09603123.2021.2013453.
[89] A. Sheikhmohammadi, E. Asgari, B. Hashemzadeh, Photo-catalytic degradation of ciprofloxacin by UV/ZnO/SO_3 process: performance, kinetic, degradation pathway, energy consumption and total cost of system, Intern. J. Environ. Anal. Chem. 103 (2023) 5296–5310, https://doi.org/10.1080/03067319.2021.1937616.
[90] R. Hassan, A. Sheikhmohammadi, E. Asgari, Efficient destruction of metronidazole and ofloxacin antibiotics in the aqueous solutions by a new advanced oxidation

process based on sulphite, Intern. J. Environ. Anal. Chem. 103 (2023) 7082–7101, https://doi.org/10.1080/03067319.2021.1965598.
[91] Y. Liu, J. Wang, Y. Wang, C. Chen, X. Wang, Z. Xiang, Sonocatalytic degradation of ciprofloxacin by BiOBr/$BiFeO_3$, Appl. Catal. A-Gen. 643 (2022) 118776, https://doi.org/10.1016/j.apcata.2022.118776.
[92] T.J. Al-Musawi, N. Mengelizadeh, K. Sathishkumar, S. Mohebi, D. Balarak, Preparation of $CuFe_2O_4$/montmorillonite nanocomposite and explaining its performance in the sonophotocatalytic degradation process for ciprofloxacin, Colloid Interface Sci. 45 (2021) 100532, https://doi.org/10.1016/j.colcom.2021.100532.
[93] T.J. Al-Musawi, N. Mengelizadeh, A.I. Alwared, D. Balarak, R. Sabaghi, Photocatalytic degradation of ciprofloxacin by MMT/$CuFe_2O_4$ nanocomposite: characteristics, response surface methodology, and toxicity analyses, Environ. Sci. Pollut. Res. 30 (2023) 70076–70093, https://doi.org/10.1007/s11356-023-27277-7.
[94] N. Neghi, R.K. Navneeth, K. Mathava, Analysis of metronidazole removal and micro-toxicity in photolytic systems: Effects of persulfate dosage, anions and reactor operation-mode, J. Environ. Chem. Eng. 6 (2018) 754–761, https://doi.org/10.1016/j.jece.2017.12.072.
[95] S.A. Dingsdag, H. Neil, Metronidazole: an update on metabolism, structure–cytotoxicity and resistance mechanisms, J. Antimicrob. Chemoth. 73 (2018) 265–279, https://doi.org/10.1093/jac/dkx351.
[96] Yu Gao, X. Zhong, X. Ren, F. Tian, N. Gao, C. Li, Synergistic mechanism and toxicity reduction potential in medium-pressure UV/chlorine/TiO_2 system for metronidazole removal, J. Water Process Eng. 65 (2024) 105903, https://doi.org/10.1016/j.jwpe.2024.105903.
[97] Y. Wang, A. Gómez-Avilés, S. Zhang, J.J. Rodriguez, J. Bedia, C. Belver, Metronidazole photodegradation under solar light with UiO-66-NH_2 photocatalyst: mechanisms, pathway, and toxicity assessment, J. Environ. Chem. Eng. 11 (2023) 109744, https://doi.org/10.1016/j.jece.2023.109744.
[98] J. Zeng, J. Liu, W. Su, J. Tang, Z. Luo, F. Tang, X. Yang, Persulfate activation by sulfide-modified nanoscale zero-valent iron for metronidazole degradation: Mechanism, major radicals and toxicity assessment, J. Water Process Eng. 53 (2023) 103733, https://doi.org/10.1016/j.jwpe.2023.103733.